

1 **Rheologic constraints on the upper mantle from five years of**
2 **postseismic deformation following the El Mayor-Cucapah**
3 **earthquake**

4 **T. T. Hines¹, E. A. Hetland¹**

5 ¹Department of Earth and Environmental Sciences, University of Michigan, Ann Arbor, Michigan, USA.

6 **Key Points:**

- 7 • Transient postseismic deformation can be observed following the El Mayor-Cucapah
8 earthquake at epicentral distances of up to 400 km
9 • Near-field postseismic deformation exhibits early transience that decays to a sustained
10 rate which is elevated above the preseismic trend
11 • Far-field postseismic deformation can be explained with a Zener or Burgers rheology
12 upper mantle

13 **Abstract**

14 We analyze five years of Southern California GPS data following the Mw=7.2 El Mayor-Cucapah
 15 earthquake. We observed transient postseismic deformation which persists for three years at
 16 epicentral distances greater than ~ 200 km. In the near-field, rapid postseismic transience de-
 17 cays to a sustained rate which exceeds its preseismic trend. We attempt to determine the mech-
 18 anisms driving this deformation, where we consider afterslip at seismogenic depths and vis-
 19 coelastic relaxation in the lower crust and upper mantle as candidate mechanisms. We find that
 20 early, rapid, near-field deformation can be explained with afterslip on the fault that ruptured
 21 coseismically, while the later, sustained, near-field deformation can be explained with either
 22 continued afterslip in an effectively elastic lower crust, or lower crustal viscoelastic relaxation
 23 with a steady-state viscosity of $\sim 10^{19}$ Pa s. The later postseismic deformation in the far-field
 24 is best explained with a transient viscosity of $\sim 10^{18}$ Pa s in the upper mantle. We argue that
 25 a transient rheology in the mantle is preferable over a Maxwell rheology because it better pre-
 26 dicted the decay in postseismic deformation, and also because it does not conflict with the gen-
 27 erally higher, steady-state viscosities inferred from studies of geophysical processes occurring
 28 over longer time-scales.

29 **1 Introduction**

30 Ground deformation in the years following a large ($Mw \gtrsim 7$) earthquake can be used to
 31 gain insight into the mechanical behavior of the crust and upper mantle. The interpretations
 32 of postseismic deformation are not always conclusive because multiple postseismic deforma-
 33 tion mechanisms, such as afterslip or viscoelastic relaxation in the lower crust and upper man-
 34 tle, can have qualitatively similar surface expressions [e.g. Savage, 1990]. This non-uniqueness
 35 complication can potentially be remedied if the postseismic deformation occurs in an area that
 36 is sufficiently well instrumented with GPS stations [Hearn, 2003]. Owing to the dense geode-
 37 metic network deployed throughout the 2000s as part of the Plate Boundary Observatory, the post-
 38 seismic deformation following the April 4, 2010, Mw=7.2 El Mayor-Cucapah earthquake in
 39 Baja California was observed at more GPS stations than any other earthquake in California
 40 to date (see Hauksson *et al.* [2011] and Fletcher *et al.* [2014] for a detailed description of this
 41 earthquake and its seismotectonic context). With such a large collection of data, we attempt
 42 to discern the mechanisms driving the postseismic deformation.

43 Previous studies which have modeled postseismic deformation following the El Mayor-
 44 Cucapah earthquake include Pollitz *et al.* [2012], Gonzalez-Ortega *et al.* [2014], Spinler *et al.*
 45 [2015], and Rollins *et al.* [2015]. Of these studies, Gonzalez-Ortega *et al.* [2014] and Rollins
 46 *et al.* [2015] have attempted to describe the postseismic deformation with afterslip in an elas-
 47 tic half-space. Gonzalez-Ortega *et al.* [2014] described five months of postseismic deforma-
 48 tion, observed by InSAR and GPS stations within ~ 50 km of the rupture, with afterslip and
 49 contraction on the coseismically ruptured fault. Gonzalez-Ortega *et al.* [2014] noted that their
 50 preferred model underestimated the GPS displacements for stations $\gtrsim 25$ km from the rup-
 51 ture and suggested that it could be the result of unmodeled viscoelastic relaxation. Using only
 52 continuous GPS stations, which are mostly north of the rupture zone, Rollins *et al.* [2015] found
 53 that three years of postseismic deformation can be adequately explained by afterslip, albeit with
 54 an implausibly large amount of slip inferred on the least constrained, southern-most fault seg-
 55 ment. Here, we suggest the afterslip inferred by Rollins *et al.* [2015] may have been acting as
 56 a proxy for distributed relaxation in the upper mantle.

57 Pollitz *et al.* [2012], Rollins *et al.* [2015] and Spinler *et al.* [2015] explored viscoelastic
 58 relaxation in the lower crust and upper mantle as a potential postseismic deformation mech-
 59 anism. The rheology of the crust and mantle is largely unknown and so modeling postseis-
 60 mic deformation with viscoelastic relaxation requires one to assume a rheologic model and
 61 then find the best fitting rheologic parameters. The inference of these rheologic parameters is
 62 a computationally expensive non-linear inverse problem which is typically approached with
 63 a forward modeling grid search method. Consequently, a simplified structure for the Earth must

be assumed in order to minimize the number of rheologic parameters that need to be estimated. For example, it is commonly assumed that the lower crust and upper mantle are homogeneous, Maxwell viscoelastic layers, which may be too simplistic for postseismic studies [Riva and Govers, 2009; Hines and Hetland, 2013]. To further reduce the dimensions of the model space, it is also necessary to make simplifying assumptions about the behavior of afterslip. For example, one can assume a frictional model for afterslip and parametrize afterslip in terms of the unknown rheologic properties of the fault [e.g. Johnson *et al.*, 2009; Johnson and Segall, 2004]. One can also assume that afterslip does not persist for more than a few months and then model the later postseismic deformation assuming it to be the result of only viscoelastic relaxation [e.g. Pollitz *et al.*, 2012; Spinler *et al.*, 2015]. However, afterslip in similar tectonic settings has been observed to persist for decades following earthquakes [Cakir *et al.*, 2012; Cetin *et al.*, 2014]. Indeed, the preferred viscoelastic model from Pollitz *et al.* [2012] significantly underestimates deformation in the Imperial Valley, which could be indicative of unmodeled continued afterslip. Neglecting to allow for sustained afterslip as a postseismic mechanism could then lead to biased inferences of viscosities.

In this study, we perform a kinematic inversion for fault slip, allowing it to persist throughout the postseismic period, while simultaneously estimating the viscosity of the lower crust and upper mantle. We create an initial model of the fault slip and effective viscosity necessary to describe early postseismic deformation using the method described in Hines and Hetland [2016]. This method uses a first-order approximation of surface deformation resulting from viscoelastic relaxation which is only applicable to the early postseismic period. In this case, our initial model describes the first 0.8 years of postseismic deformation following the El Mayor-Cucapah earthquake. We then use the inferred effective viscosity structure from the initial model to create a suite of postseismic models which we test against the five years of postseismic data available to date. Of the suite of models tested, we find that postseismic deformation following the El Mayor-Cucapah earthquake can be explained with a combination of afterslip on a fault segment running through the Sierra Cucapah and viscoelastic relaxation in a Zener rheology upper mantle with a transient viscosity on the order of 10^{18} Pa s.

2 Data Processing

We use continuous GPS position time series provided by University Navstar Consortium (UNAVCO) for stations within a 400 km radius about the El Mayor-Cucapah epicenter. We collectively describe the coseismic and postseismic displacements resulting from the El Mayor-Cucapah earthquake as $u_{\text{post}}(t)$. We consider the GPS position time series, $u_{\text{obs}}(t)$, to be the combination of $u_{\text{post}}(t)$, secular tectonic deformation, annual and semi-annual oscillations, and coseismic offsets from significant earthquakes over the time span of this study. The June 14, 2010, Mw=5.8 Ocotillo earthquake and the Brawley swarm, which included an Mw=5.5 and an Mw=5.4 event on August 26, 2012 (Figure 1), are the only earthquakes that produced noticeable displacements in any of the time series. We treat the displacements resulting from the Brawley swarm as a single event because the daily solutions provided by UNAVCO cannot resolve the separate events. Although the Ocotillo earthquake had its own series of aftershocks [Hauksson *et al.*, 2011], neither the Ocotillo earthquake nor the Brawley swarm produced detectable postseismic deformation. We model displacements resulting from these events with only a Heaviside function, $H(t)$, describing the coseismic offsets. We then model $u_{\text{obs}}(t)$ as

$$u_{\text{obs}}(t) = u_{\text{pred}}(t) + \epsilon, \quad (1)$$

where

$$\begin{aligned} u_{\text{pred}}(t) = & u_{\text{post}}(t)H(t - t_{\text{emc}}) + c_0 + c_1 t + \\ & c_2 \sin(2\pi t) + c_3 \cos(2\pi t) + c_4 \sin(4\pi t) + c_5 \cos(4\pi t) + \\ & c_6 H(t - t_{\text{oc}}) + c_7 H(t - t_{\text{bs}}). \end{aligned} \quad (2)$$

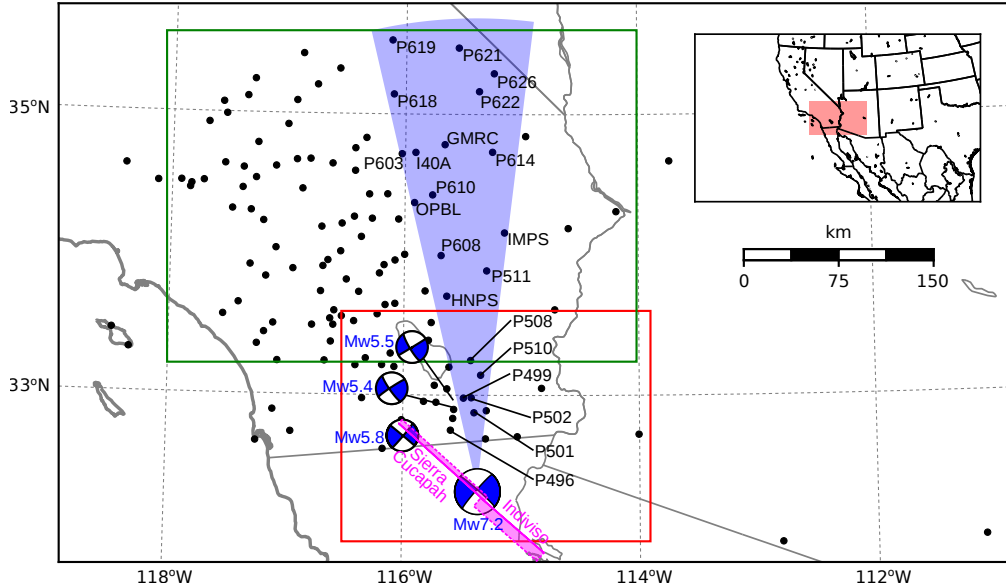


Figure 1. Map of the region considered in this study. The large focal mechanism is the GCMT solution for the El Mayor-Cucapah earthquake, and the three small focal mechanisms are for the Ocotillo earthquake and the two main shocks during the Brawley swarm. The black dots indicate the locations of GPS stations used in this study. The fault geometry used in this study is shown in magenta where dashed lines indicate buried edges of the fault segments. The green and red boxes demarcate the extent of the near-field and far-field maps (Figures 4 and 5). Stations inside the blue sector, which highlights the area within 10° of the El Mayor-Cucapah P-axis, are used in Figures 7 and 10.

In the above equations, t_{emc} , t_{oc} and t_{bs} are the times of the El Mayor-Cucapah earthquake, Ocotillo earthquake, and the Brawley swarm, respectively, c_0 through c_7 are unknown coefficients, and ϵ is the observation noise. We are using years as our unit of time which makes c_2 through c_5 the coefficients for annual and semi-annual oscillations. We only estimate jumps associated with the Ocotillo earthquake and Brawley swarm for stations within 40 km of their epicenters.

Stations which recorded displacements that clearly cannot be described by the aforementioned processes are not included in our analysis. This includes stations in the Los Angeles basin, where anthropogenic deformation can be larger than the postseismic signal that we are trying to estimate [Bawden *et al.*, 2001; Argus *et al.*, 2005]. In order to ensure an accurate estimation of the secular deformation, we only use stations that were installed at least six months prior to El Mayor-Cucapah earthquake even though several GPS stations were installed after the earthquake to get better coverage of the postseismic deformation field [Spiner *et al.*, 2015]. It would be possible to subtract secular velocities derived from elastic block models [e.g. Meade and Hager, 2005] from velocities recorded at the newly installed stations to get an estimate of postseismic velocities at those stations. However, estimating velocities from an already noisy displacement time series can introduce significant uncertainties depending on exactly how the estimation is done. We therefore use coseismic and postseismic displacements, rather than velocities, in our inverse method described in Section 3. This choice prevents us from using the newly installed stations for our analysis.

The October 16, 1999, Mw=7.1 Hector Mine earthquake, which occurred \sim 270 km north of the El Mayor-Cucapah epicenter, produced transient postseismic deformation which we do not wish to model, either mechanically or through empirical line fitting. We thus restrict our analysis to deformation observed six years after the Hector Mine earthquake, which is when

139 postseismic velocities at sites near the Hector Mine epicenter are approximately constant [Savage
 140 and Svare, 2009]. When appraising our model fit in Section 3, we see some systematic
 141 residuals in the vicinity of the Hector Mine epicenter, which may be the result of errors in the
 142 assumption that the trend in Hector Mine postseismic deformation is linear after six years.

143 Studies of postseismic deformation typically assume a parametric form for $u_{\text{post}}(t)$, such
 144 as one with a logarithmic or exponential time dependence [e.g. Savage *et al.*, 2005]. However,
 145 by assuming a logarithmic or exponential form of $u_{\text{post}}(t)$ we run the risk of over fitting the
 146 GPS time series and inferring a non-existent postseismic signal. We therefore do not assume
 147 any parametric form for $u_{\text{post}}(t)$ and rather treat it as integrated Brownian motion, so that

$$\dot{u}_{\text{post}}(t) = \sigma^2 \int_0^t w(s)ds, \quad (3)$$

148 where $w(t)$ is white noise and the variance of $\dot{u}_{\text{post}}(t)$ increases linearly with time by a factor
 149 of σ^2 . We use a Kalman filtering approach to estimate $u_{\text{post}}(t)$ and the unknown parameters
 150 in eq. (2). In the context of Kalman filtering, our time varying state vector is

$$\mathbf{X}(t) = [u_{\text{post}}(t), \dot{u}_{\text{post}}(t), c_0, \dots, c_7] \quad (4)$$

151 and eq. (2) is the observation function which maps the state vector to the GPS observations.
 152 We initiate the Kalman filter by assuming a prior estimate of $\mathbf{X}(t)$ at the first time epoch, denoted
 153 $\mathbf{X}_{1|0}$, which has a sufficiently large covariance, denoted $\Sigma_{1|0}$, to effectively make our
 154 prior uninformed. For each time epoch, t_i , Bayesian linear regression is used to incorporate
 155 GPS derived estimates of displacement with our prior estimate of the state, $\mathbf{X}_{i|i-1}$, to form
 156 a posterior estimate of the state, $\mathbf{X}_{i|i}$, which has covariance $\Sigma_{i|i}$. We then use the posterior
 157 estimate of the state at time t_i to form a prior estimate of the state at time t_{i+1} through the
 158 transition function

$$\mathbf{X}_{i+1|i} = \mathbf{F}_{i+1} \mathbf{X}_{i|i} + \delta_{i+1}, \quad (5)$$

159 where

$$\mathbf{F}_{i+1} = \begin{bmatrix} 1 & (t_{i+1} - t_i) & \mathbf{0} \\ 0 & 1 & \mathbf{0} \\ \mathbf{0} & \mathbf{0} & \mathbf{I} \end{bmatrix} \quad (6)$$

160 and δ_{i+1} is the process noise, which has zero mean and covariance described by

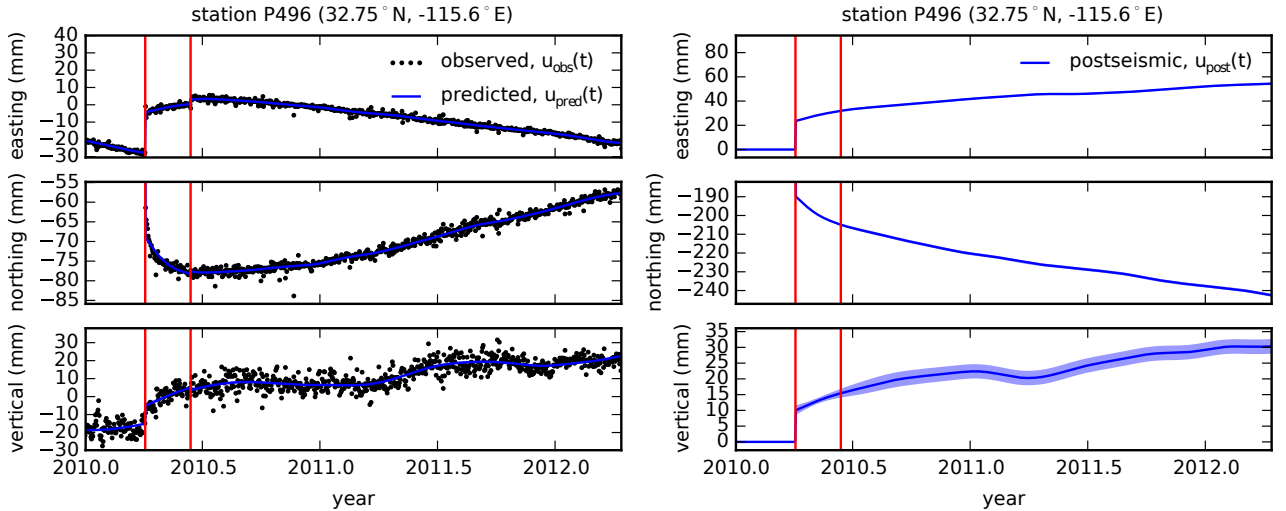
$$\mathbf{Q}_{i+1} = \sigma^2 \begin{bmatrix} \frac{(t_{i+1}-t_i)^3}{3} & \frac{(t_{i+1}-t_i)^2}{2} & \mathbf{0} \\ \frac{(t_{i+1}-t_i)^2}{2} & (t_{i+1} - t_i) & \mathbf{0} \\ \mathbf{0} & \mathbf{0} & \mathbf{0} \end{bmatrix}. \quad (7)$$

161 The covariance of the new prior state, $\mathbf{X}_{i+1|i}$, is then described by

$$\Sigma_{i+1|i} = \mathbf{F}_{i+1} \Sigma_{i|i} \mathbf{F}_{i+1}^T + \mathbf{Q}_{i+1}. \quad (8)$$

162 This process is repeated for each of the N time epochs at which point we use Rauch-Tung-
 163 Striebel smoothing [Rauch *et al.*, 1965] to find $\mathbf{X}_{i|N}$, which is an estimate of the state at time
 164 t_i that incorporates GPS observation for all N time epochs. Our final estimates of $u_{\text{post}}(t)$
 165 are used in subsequent analysis, while the remaining components of the state vector are con-
 166 sidered nuisance parameters. In the interests of computational tractability, we down sample
 167 our smoothed time series from daily solutions down to weekly solutions.

168 The smoothness of $u_{\text{post}}(t)$ is controlled by the chosen value of σ^2 , which describes how
 169 rapidly we expect postseismic displacements to vary over time. Setting σ^2 equal to zero will



186 **Figure 2.** Left panels show GPS time series from UNAVCO (black) and the predicted displacement (blue)
 187 from eq. (2) for a near-field station. Red lines indicate the times of the El Mayor-Cucapah and Ocotillo earth-
 188 quake. The right panels show estimated coseismic and postseismic displacements, u_{post} , which are extracted
 189 from the predicted displacements. The 68% confidence interval is shown in light blue.

170 effectively result in modeling $u_{\text{post}}(t)$ as a straight line which is insufficient to describe the
 171 expected transient behavior in postseismic deformation. The other end member, where σ^2 is
 172 infinitely large, will result in $u_{\text{pred}}(t)$ over fitting the data. While one can use a maximum like-
 173 lihood based approach for picking σ^2 [e.g. Segall and Mathews, 1997], we instead take a sub-
 174 jective approach and choose a value for σ^2 that is just large enough to faithfully describe the
 175 observed deformation at the most near-field station in our study, P496, which exhibits the most
 176 rapid changes in velocity. This ensures that σ^2 will be sufficiently large so that our estimate
 177 of $u_{\text{post}}(t)$ does not smooth out potentially valuable postseismic signal at the remaining sta-
 178 tions. We find that using $\sigma^2 = 0.05 \text{ m}^2/\text{yr}^3$ adequately describes all but the first week of post-
 179 seismic deformation at station P496, which slightly increases our estimate of coseismic dis-
 180 placements (Figure 2). We include an example of estimating $u_{\text{post}}(t)$ for a far-field station,
 181 P619, which is about 359 km north of the El Mayor-Cucapah epicenter (Figure 3). At station
 182 P619, along with all the other stations in the Mojave region, there is a south-trending post-
 183 seismic transience that persists for the first three years after the El Mayor-Cucapah earthquake.
 184 Postseismic deformation that extends to these epicentral distances has also been observed af-
 185 ter the Hector Mine earthquake [Freed et al., 2007].

191 It is important to note that the shown uncertainties in $u_{\text{post}}(t)$ do not account for the non-
 192 negligible epistemic uncertainty in eq. (2). For example, we assume a constant rate of secu-
 193 lar deformation, which appears to be an appropriate approximation for all but perhaps the sta-
 194 tions closest to the Hector Mine epicenter, as noted above. Also, our model for seasonal de-
 195 formation in eq. (2) assumes a constant amplitude over time, which means that any yearly vari-
 196 ability in the climatic conditions could introduce systematic residuals [Davis et al., 2012]. In-
 197 deed, it would be more appropriate to consider the seasonal amplitudes $c_2 - c_5$ in eq. (2) as
 198 stochastic variables [Murray and Segall, 2005]. By using constant seasonal amplitudes, our es-
 199 timate of $u_{\text{post}}(t)$ seems to describe some of the unmodeled annual and semi-annual oscilla-
 200 tions (e.g. Figure 3).

201 We show in Figures 4 and 5 the near and far-field postseismic displacements accumu-
 202 lated over the time intervals 0–1 years, 1–3 years, and 3–5 years, as well as the coseismic dis-
 203 placements. Stations at epicentral distances beyond ~ 200 km have an elevated rate of defor-
 204 mation for the first three years following the earthquake. This far-field deformation is trend-

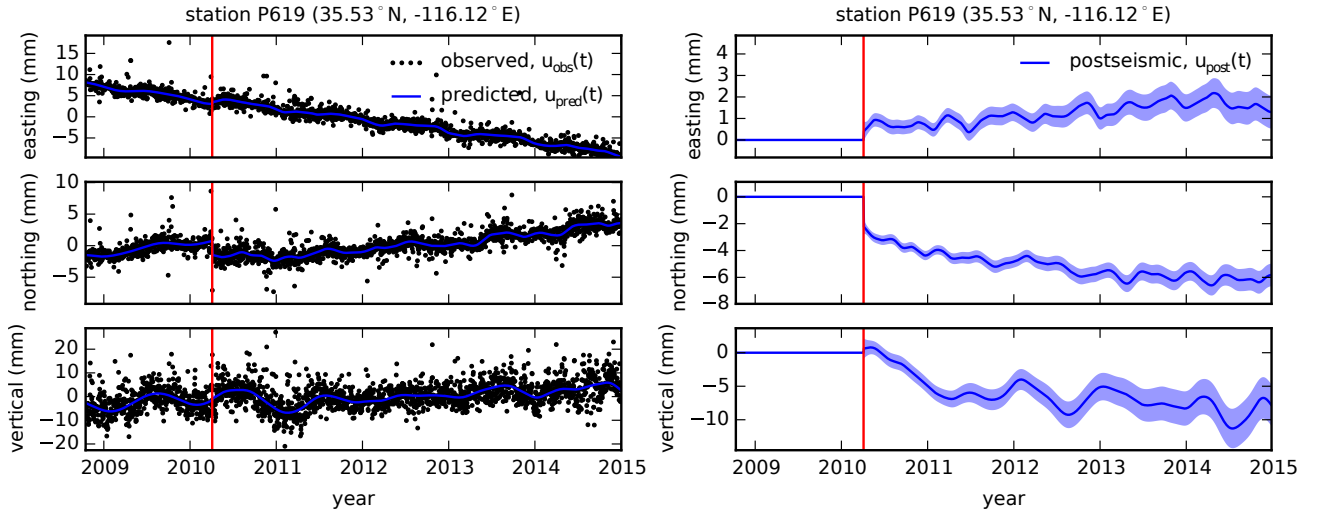


Figure 3. same as Figure 2 but for a far-field station.

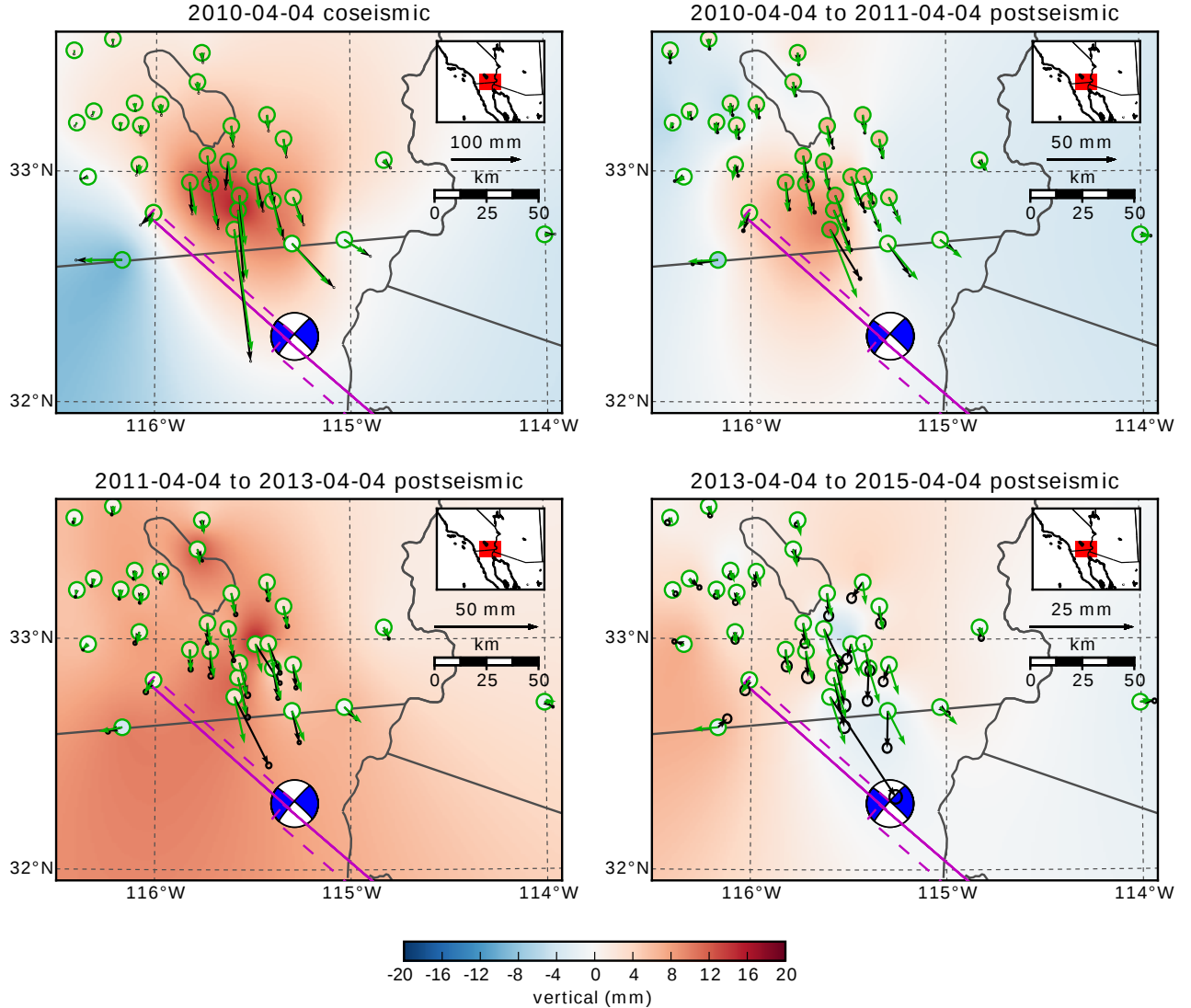
ing southward at a rate of a few millimeters per year along the direction of the El Mayor-Cucapah P-axis. A similar eastward trend can be seen in the few far-field stations in Arizona, located along the T-axis. After three years, the trend in far-field postseismic deformation is barely perceptible. Most far-field stations display an initial subsidence for the first year after the El Mayor-Cucapah earthquake followed by continued uplift. This trend in vertical deformation can be observed in all three of the quadrants where postseismic data is available, which means that the vertical deformation does not exhibit an anti-symmetric quadrant pattern, as would be expected for postseismic processes. Although we use vertical deformation in our analysis in Section 3, we do not put an emphasis on trying to describe the vertical deformation because it likely does not have postseismic origins.

The near-field postseismic deformation is notably sustained when compared to the far-field deformation. Namely, the station in this study which is closest to the El Mayor-Cucapah epicenter, P496, has a steady postseismic trend of ~ 1.5 cm/yr to the south after about one year. Vertical postseismic deformation in the near-field does display a quadrant pattern which is consistent with the coseismic vertical deformation, suggesting that it is resulting from postseismic processes. However, the vertical postseismic signal is only apparent for the first year after the earthquake (Figure 4). As with the far-field deformation, there is a general trend of uplift in the near-field after about one year.

3 Postseismic Modeling

We seek to find the mechanisms driving five years of postseismic deformation following the El Mayor-Cucapah earthquake and we consider afterslip and viscoelastic relaxation as candidate mechanisms. Poroelastic rebound has also been used to model postseismic deformation [e.g. Jónsson *et al.*, 2003]; however, Gonzalez-Ortega *et al.* [2014] found that poroelastic rebound is unlikely to be a significant contributor to postseismic deformation following the El Mayor-Cucapah earthquake. Furthermore, we consider stations which are sufficiently far away from the rupture that poroelastic rebound should be insignificant.

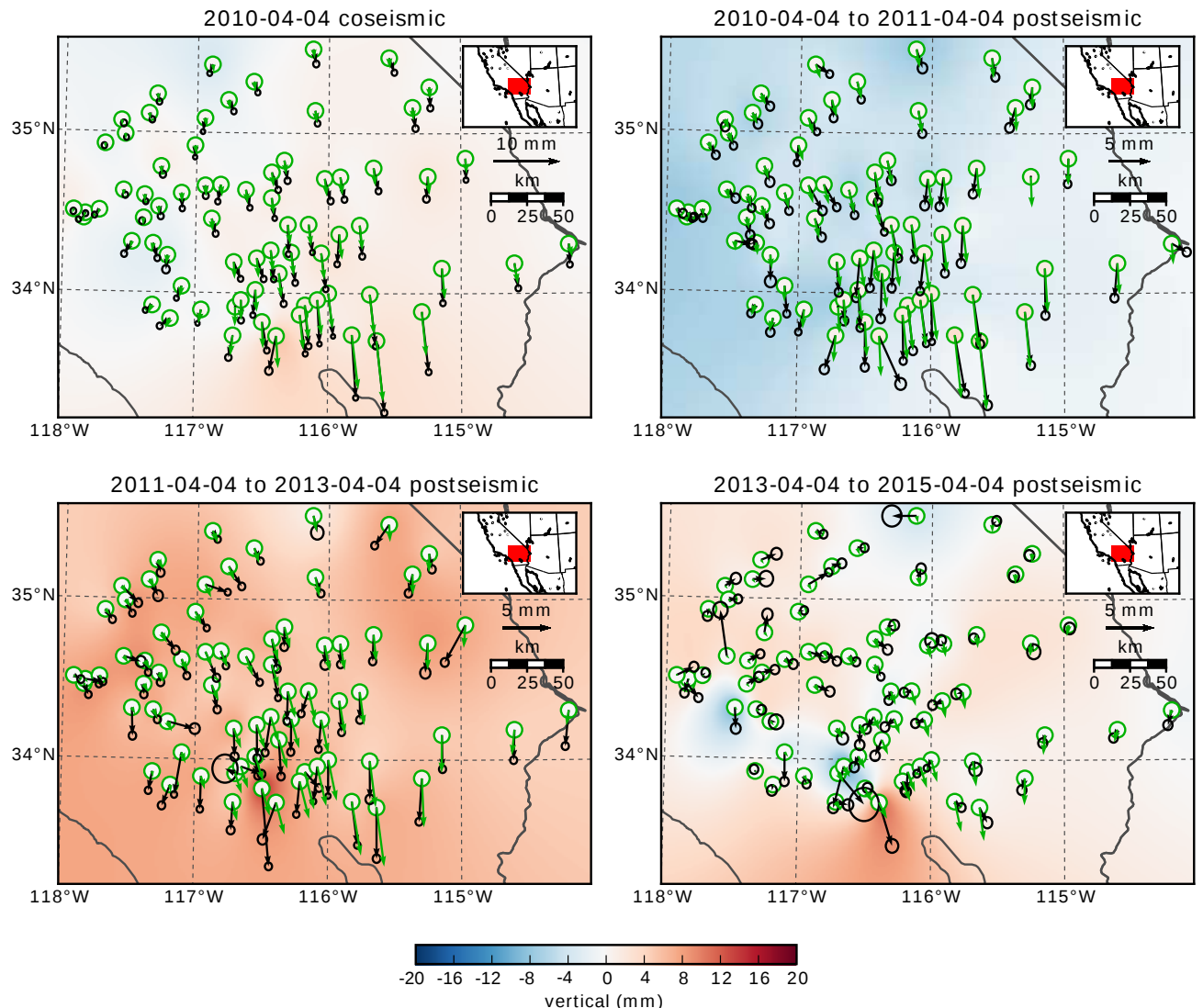
We estimate coseismic and time-dependent postseismic fault slip, both of which are assumed to occur on a fault geometry modified from Wei *et al.* [2011b]. Field studies [Fletcher *et al.*, 2014] and LIDAR observations [Oskin *et al.*, 2012] have revealed a significantly more complicated fault geometry than what was inferred by Wei *et al.* [2011b], especially within the Sierra Cucapah. However, we find that a relatively simple coseismic fault geometry based on



215 **Figure 4.** Near-field coseismic and cumulative postseismic displacements over the indicated time periods
 216 (black) and predicted displacements for our preferred model from Section 3.3 (green). The black error ellipses
 217 show the 68% confidence interval for the observed horizontal displacements. Observed vertical displacements
 218 are shown as an interpolated field and predicted vertical displacements are shown within the green circles.
 219 Note that the interpolant is not well constrained in Mexico where there is no data available.

depth (km)	λ (GPa)	μ (GPa)	η_{eff} (10^{18} Pa s)	μ_k/μ
0-5	24.0	24.0	-	-
5-15	35.0	35.0	-	-
15-30	42.0	42.0	44.3	0.0
30-60	61.0	61.0	5.91	0.375
60-90	61.0	61.0	1.99	0.375
90-120	61.0	61.0	1.31	0.375
120-150	61.0	61.0	1.10	0.375
150-∞	61.0	61.0	1.07	0.375

230 **Table 1.** Assumed and estimated material properties. λ and μ are assumed known *a priori* and are based
 231 on the values used for the coseismic model by Wei *et al.* [2011b]. The values for η_{eff} are estimated in Section
 232 3.2, and μ_k/μ are the optimal shear moduli ratios found in Section 3.3 for a Zener rheology upper mantle.

**Figure 5.** Same as Figure 4 but for far-field stations.

[Wei *et al.*, 2011b] is adequate because most of the stations used in this study are sufficiently far from the El Mayor-Cucapah rupture that they are insensitive to the details in the fault geometry found by Fletcher *et al.* [2014] and Osokin *et al.* [2012]. The fault geometry used in this study (Figure 1) consists of the two main fault segments inferred by Wei *et al.* [2011b], where the northern segment runs through the Sierra Cucapah up to the US-Mexico border and the southern segment is the Indiviso fault which extends down to the Gulf of California. Both segments extend from the surface to 15 km depth. We extend the northern segment by 40 km to the northwest, which is motivated by the clustering of aftershocks on the northern tip of the coseismic rupture zone [Hauksson *et al.*, 2011; Kroll *et al.*, 2013]. This extended fault segment was also found to be necessary by Rollins *et al.* [2015] and Pollitz *et al.* [2012] in order to describe the postseismic deformation.

256 3.1 Elastic Postseismic Inversion

We consider a variety of rheologic models for the lower crust and upper mantle. The simplest rheologic model is to consider them to be effectively elastic and isotropic. In such case, the rheologic parameters consist of the Lamé parameters, λ and μ , which are reasonably well known and we use the same values used by Wei *et al.* [2011b] throughout this paper (Table 1). The only unknown is the distribution of fault slip, which can be easily estimated from postseismic deformation through linear least squares. Rollins *et al.* [2015] used a subset of the GPS stations considered in this study and found that three years of postseismic deformation following the El Mayor-Cucapah earthquake can be explained with afterslip on the coseismic fault plane without requiring any viscoelastic relaxation. We also perform an elastic slip inversion, but we use GPS stations within a larger radius about the El Mayor-Cucapah epicenter (400 km instead of \sim 200 km). Our forward problem describing predicted postseismic deformation, u_{pred} , in terms of time dependent fault slip, s , is

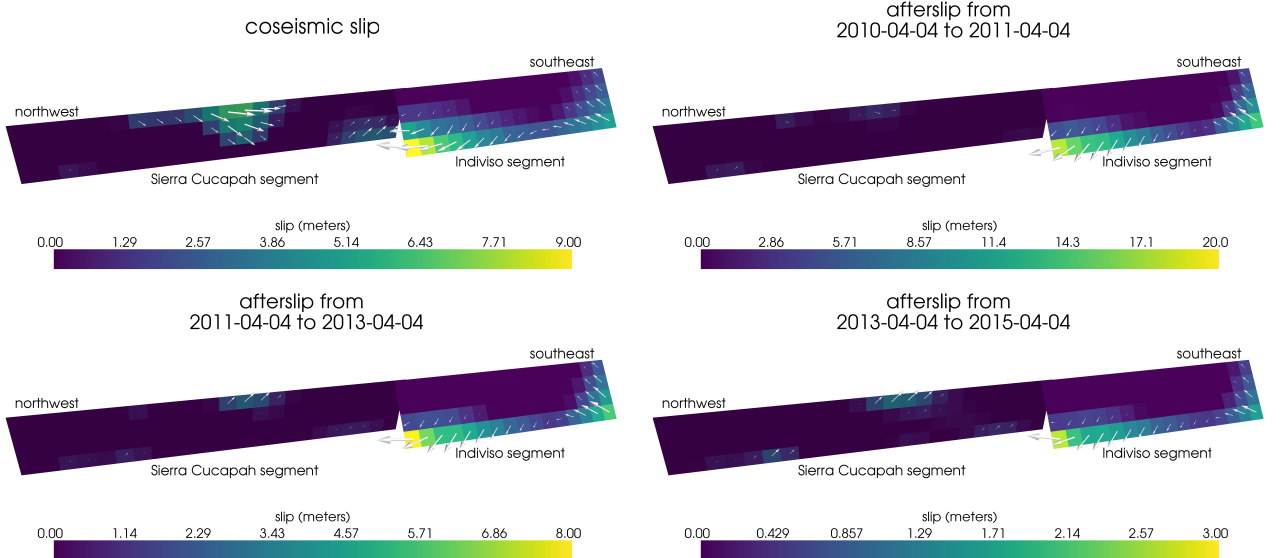
$$268 \quad u_{\text{pred}}(x, t) = \int_F s(\xi, t) g(x, \xi) d\xi, \quad (9)$$

where F denotes the fault and $g(x, \xi)$ is the elastic Green's function describing displacement at surface position x resulting from slip at ξ on the fault. We estimate coseismic slip and the rate of afterslip over the postseismic time intervals 0.0-0.125, 0.125-0.25, 0.25-0.5, 0.5-1.0, 1.0-2.0, 2.0-3.0, 3.0-4.0, and 4.0-5.0 years. Each fault segment is discretized into roughly 4 km by 4 km patches and we impose that the direction of slip and slip rate are within 45° of right-lateral. We also add zeroth-order Tikhonov regularization so that our solution for s satisfies

$$275 \quad \min_s \left(\left\| \frac{u_{\text{pred}}(s) - u_{\text{post}}}{\sigma_{\text{post}}} \right\|_2^2 + \lambda_s \|s\|_2^2 \right), \quad (10)$$

where σ_{post} is the uncertainty on postseismic displacements and λ_s is a penalty parameter which is chosen with a trade-off curve. We use Pylith [Aagaard *et al.*, 2013] to compute the Green's functions for this inversion as well as for the remaining inversions in this paper.

Our coseismic slip and afterslip solutions are shown in Figure 6. Similar to Rollins *et al.* [2015], we find that a large amount of afterslip on the Indiviso fault segment is required to explain the observations. The potency of our inferred coseismic slip is $3.2 \times 10^9 \text{ m}^3$, equivalent to a Mw=7.28 earthquake when assuming a shear modulus of 32 GPa. The potency of our inferred cumulative five years of afterslip is $6.1 \times 10^9 \text{ m}^3$, equivalent to a Mw=7.46 earthquake, which is unrealistically large if we consider afterslip to be driven by coseismically induced stresses. Figure 7 shows the time series for the observed and predicted postseismic displacements at stations along the El Mayor-Cucapah P-axis. We show the radial component of displacements with respect to the El Mayor-Cucapah epicenter and we also rescale the displacements so that the difference between the minimum and maximum observed displacements are the same for each station. Our elastic slip model accurately describes near-field postseis-



295 **Figure 6.** Coseismic slip and cumulative afterslip over the indicated time intervals when assuming the crust
296 and mantle are elastic. Color indicates the magnitude of slip while arrows indicate the motion of the hanging
297 wall.

290 mic deformation and systematically underestimates postseismic deformation at epicentral dis-
291 tances $\gtrsim 150$ km. When the fault segments used in the inversion are extended down to 30 km
292 depth, rather than 15 km, the systematic far-field residuals are smaller but remain apparent.
293 Because an elastic model requires an unrealistic amount of afterslip and is unable to predict
294 far-field deformation, we move on to consider viscoelastic models in the next section.

307 3.2 Early Postseismic Inversion

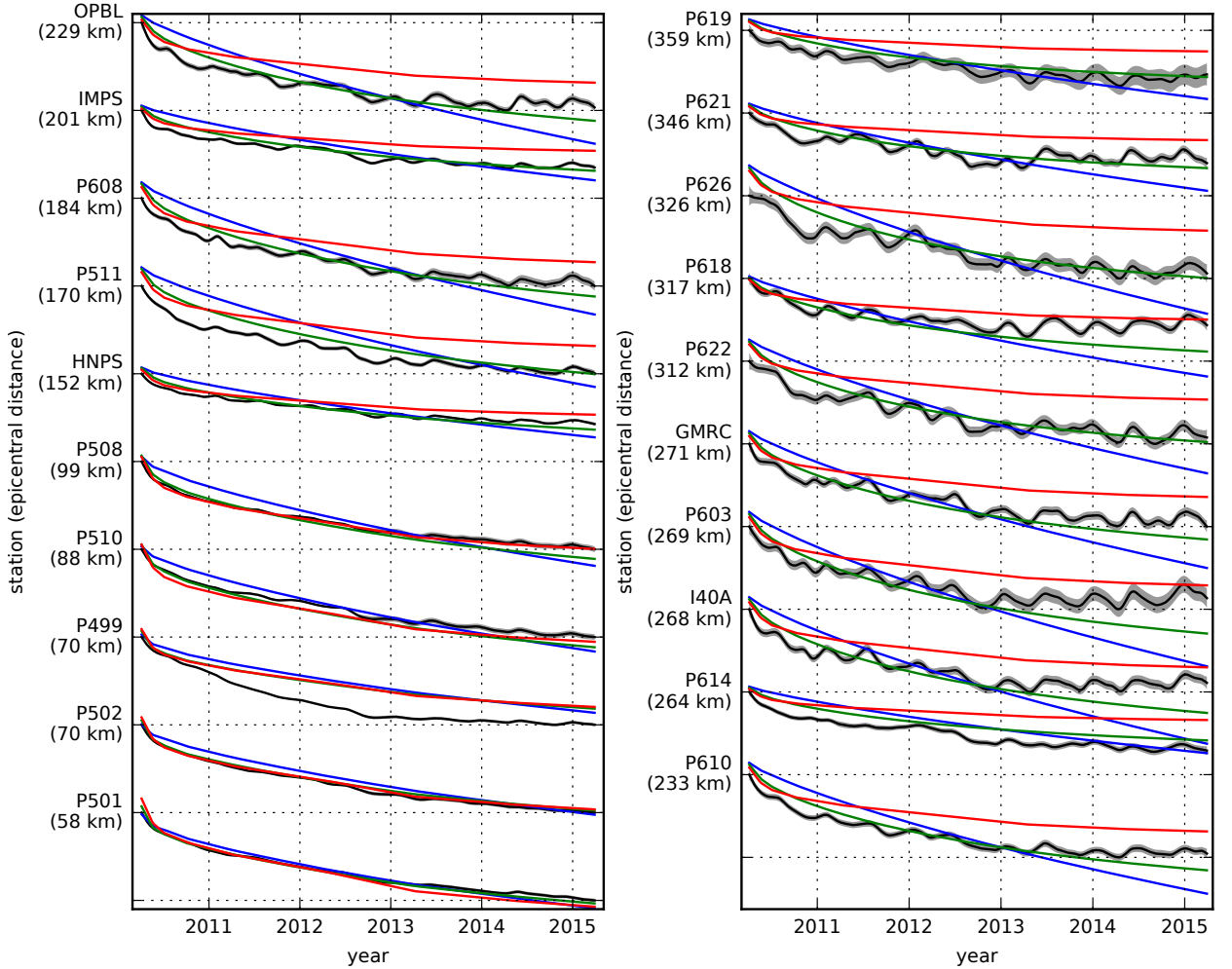
308 For any linear viscoelastic rheology of the crust and mantle, postseismic displacements
309 resulting from time dependent fault slip can be described as

$$u_{\text{pred}}(x, t) = \int_F s(\xi, t) g(x, \xi) d\xi + \int_0^t \int_F s(\xi, \tau) f(t - \tau, x, \xi) d\xi d\tau, \quad (11)$$

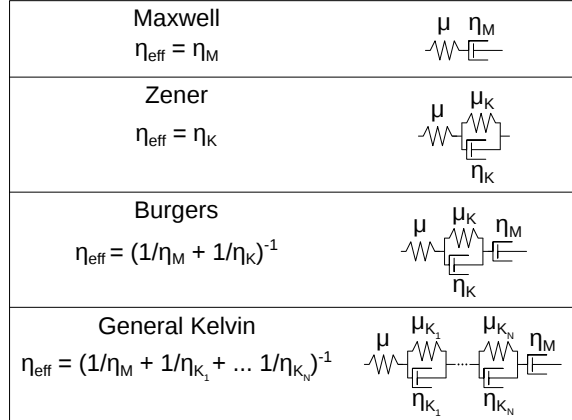
310 where $f(t, x, \xi)$ describes the time-dependent velocity at x resulting from viscoelastic relax-
311 ation of stresses induced by slip at ξ . f is a function of λ , μ , and any additional rheologic pa-
312 rameters controlling the viscoelastic response, which are generally not well known. Schematic
313 representations of the viscoelastic rheologic models considered in this study are shown in Fig-
314 ure 8. We discuss these rheologic models and their use in geophysical studies in Section 4.

317 In order to greatly simplify the inverse problem, we use the method described in *Hines*
318 and *Hetland* [2016] to constrain an initial effective viscosity structure from the early postseis-
319 mic deformation. Our method uses the fact that coseismic stresses throughout the crust and
320 upper mantle depend on the instantaneous elastic parameters and are independent of the vis-
321 coelastic parameters which we wish to estimate. Immediately following an earthquake, each
322 parcel will have a strain rate that is proportional to the coseismic stress and inversely propor-
323 tional to the parcel's effective viscosity, η_{eff} . Using one-dimensional rheologic models, we de-
324 fine the effective viscosity as

$$\eta_{\text{eff}} = \left. \frac{\sigma}{\dot{\varepsilon}} \right|_{t=0}, \quad (12)$$



298 **Figure 7.** Scaled radial component of postseismic displacements. Downward motion indicates that the
 299 station is moving toward the El Mayor-Cucapah epicenter. Displacement time series are scaled so that the
 300 minimum and maximum observed values lie on the grid lines. The observed postseismic displacements, u_{post}
 301 are shown in black with gray indicating the 68% confidence interval. The displacements predicted by the best
 302 fitting elastic model are shown in red. The blue and green lines are the predicted postseismic displacements
 303 for the models discussed in Section 3.3. The blue lines show the predicted displacements for the model with
 304 a Maxwell viscoelastic lower crust and upper mantle. The green line shows the predicted displacements
 305 for the model with a Maxwell viscoelastic lower crust and a Zener viscoelastic upper mantle. The effective
 306 viscosities are the same for both models and are shown in Figure 12.



315 **Figure 8.** Schematic illustration of the rheologic models considered in this paper as well as their effective
 316 viscosities.

325 where σ is an applied stress at $t = 0$ and $\dot{\varepsilon}$ is the resulting strain rate. Figure 8 shows how
 326 η_{eff} relates to the parameters for various linear viscoelastic rheologies. We can deduce that the
 327 initial rate of surface deformation resulting from viscoelastic relaxation is a summation of the
 328 surface deformation resulting from relaxation in each parcel, scaled by the reciprocal of the
 329 parcel's effective viscosity. That is to say

$$f(0, x, \xi) = \int_L \frac{h(x, \xi, \zeta)}{\eta_{\text{eff}}(\zeta)} d\zeta, \quad (13)$$

330 where L denotes the crust and mantle and $h(x, \xi, \zeta)$ describes the initial rate of deformation
 331 resulting from viscoelastic relaxation at ζ induced by slip at ξ . We can combine eq. (13) with
 332 eq. (11) to get a first-order approximation for early postseismic deformation,

$$u_{\text{pred}}(x, t) \approx \int_F s(\xi, t) g(x, \xi) d\xi + \int_0^t \int_F \int_L \frac{s(\tau, \xi)}{\eta_{\text{eff}}(\zeta)} h(x, \xi, \zeta) d\zeta d\xi d\tau, \quad (14)$$

333 which is valid for as long as the rate of deformation resulting from viscoelastic relaxation is
 334 approximately constant. Although eq. (14) may only be valid for a short portion of the post-
 335 seismic period, its utility becomes apparent when noting that g and h are only functions of
 336 the fault geometry and instantaneous elastic properties, λ and μ , and thus g and h can be com-
 337 puted numerically as a preprocessing step. The forward problem in eq. (14) can then be rapidly
 338 evaluated for any realization of s and η_{eff} . This is in contrast to evaluating the full forward
 339 problem, eq. (11), numerically for each realization of s and the unknown rheologic proper-
 340 ties.

341 Details on how eq. (14) is used to estimate s and η_{eff} from postseismic deformation can
 342 be found in *Hines and Hetland* [2016]. A non-linear Kalman filter based inverse method can
 343 also be used to estimate s and η_{eff} in a manner similar to *Segall and Mathews* [1997] or *McGuire*
 344 and *Segall* [2003], in which we would not have to explicitly impose a time dependent parametriza-
 345 tion of s . We have thoroughly explored Kalman filter based approaches, but we ultimately pre-
 346 fer the method described in *Hines and Hetland* [2016] because of its relative simplicity. More-
 347 over, we believe the piecewise continuous representation of slip with respect to time is suf-
 348 ficiently general for the resolving power of these GPS data.

349 We estimate coseismic slip and afterslip with the same spatial and temporal discretiza-
 350 tion as in Section 3.1. Simultaneously, we estimate η_{eff} within six vertically stratified layers
 351 which have depths ranging from 15-30 km, 30-60 km, 60-90 km, 90-120 km, 120-150 km,

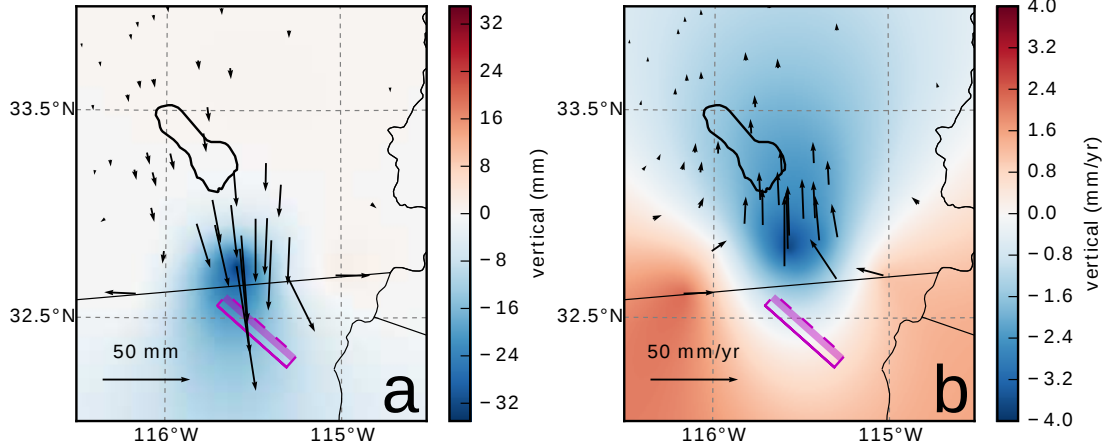
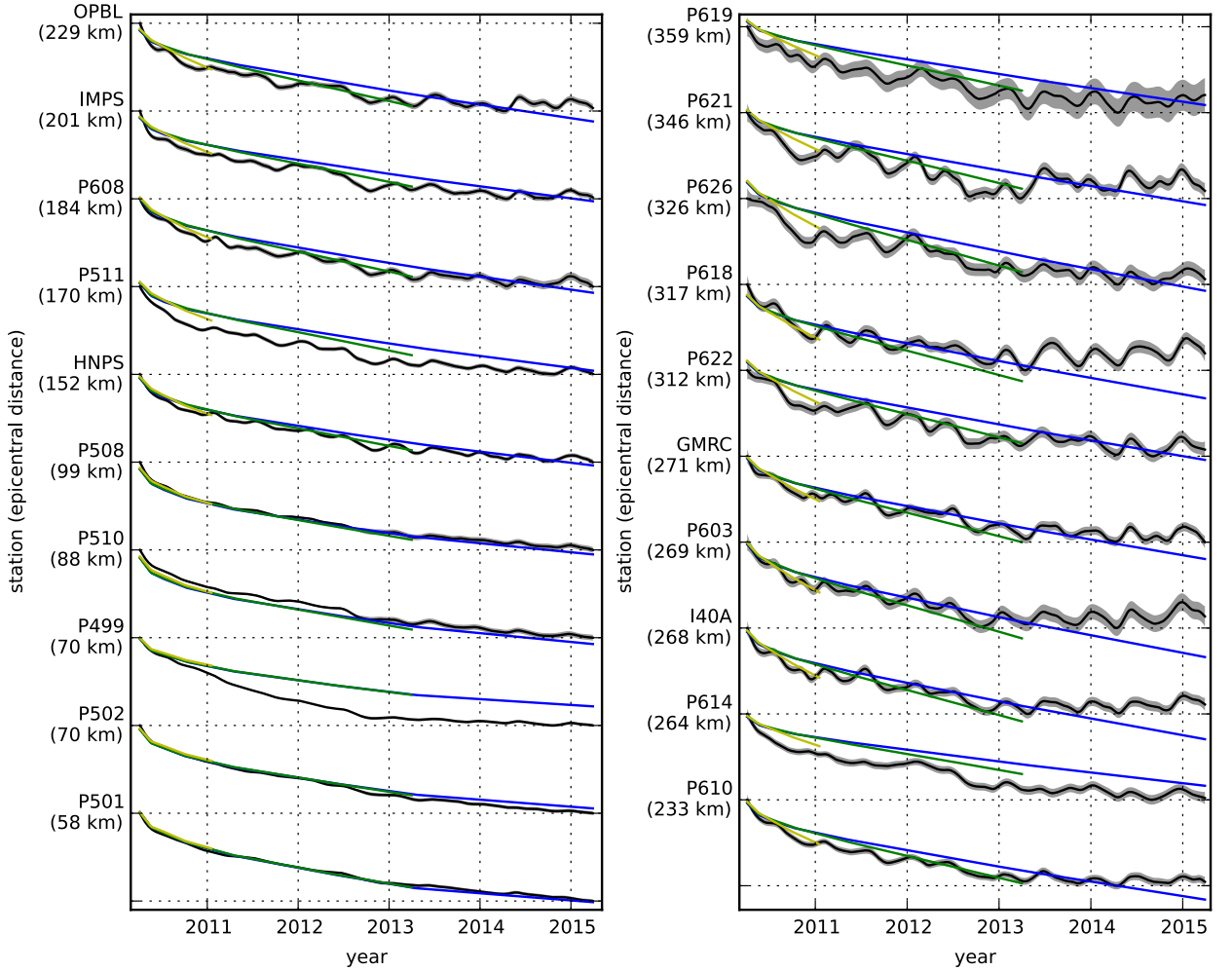


Figure 9. Displacements resulting from fault slip at lower crustal depths (a), and initial velocities resulting from subsequent relaxation of a viscoelastic lower crust (b). The fault segment dips 75° to the north-east and its surface projection is outlined in magenta. The highlighted area on the fault extends from 15 to 30 km depth and indicates where 1 meter of right-lateral slip was imposed. The elastic properties of the crust and mantle are the same as in Table 1, and η_{eff} is 10^{18} Pa s in the lower crust. Vertical displacements are interpolated between station locations.

and from 150 km to the bottom of our numerical model domain at 800 km. We again restrict fault slip to occur between 0 and 15 km depth, which is done in order to help eliminate inevitable non-uniqueness in the inversion. It is well understood that fault slip at sufficiently great depths can produce surface deformation that is indistinguishable from viscoelastic relaxation, at least in two-dimensional earthquake models [Savage, 1990]. Additionally, we note that when simultaneously estimating both afterslip and viscosity in the lower crust, the inverse problem becomes particularly ill-posed. This ill-posedness is illustrated in Figure 9, which shows the displacements resulting from a meter of slip on a fault extending from 15 to 30 km depth and the initial velocity resulting from subsequent viscoelastic relaxation in the lower crust, which is given a viscosity of 10^{18} Pa s. In this demonstration, the viscoelastic relaxation is entirely driven by the fault slip in the lower crust. The horizontal displacements from fault slip are in the opposite direction as the displacements resulting from viscoelastic relaxation. This means that surface displacements resulting from afterslip at lower crustal depths can be cancelled out, at least partially, by a low viscosity lower crust. We eliminate this null space by allowing only one mechanism in the lower crust, which we choose to be viscoelastic relaxation. This is not to say that we do not believe deep afterslip to be a possibility; rather, we restrict slip to seismogenic depths as a modeling necessity. Although, it has been noted that the pattern of vertical postseismic deformation following the El Mayor-Cucapah earthquake indicates that a significant amount of afterslip must be shallow [Rollins *et al.*, 2015].

We must determine at which point the early postseismic approximation breaks down, which we will denote as t_{bd} . As noted, eq. (14) is valid for as long as the rate of deformation resulting from viscoelastic relaxation is approximately constant. We can almost certainly assume that deformation at the most far-field stations, which are ~ 400 km away from the El Mayor-Cucapah epicenter, is the result of viscoelastic relaxation. The approximation should then be valid for as long as a linear trend adequately approximates the far-field deformation. Using this logic, it would appear that t_{bd} is about one year after the El Mayor-Cucapah earthquake. Another way to determine t_{bd} is to find the best fitting prediction of eq. (14) to observed deformation using increasing durations of the postseismic time series. t_{bd} should be the point when eq. (14) is no longer capable of describing the observed deformation without incurring systematic misfits. When using eq. (14) to fit the entire five years of postseismic displacements,



399 **Figure 10.** Observed postseismic displacements (black) and best fitting predictions of eq. (14) to 5.0 (blue),
400 3.0 (green), and 0.8 (yellow) years of the postseismic data.

388 we see that the near-field displacements (e.g., station P501) are accurately predicted. When
389 looking at displacements in the far-field (e.g., station P621), we see that eq. (14) overestimates
390 the rate of deformation in the later postseismic period and underestimates the rate of defor-
391 mation in the early period (Figure 10). Due to the low signal-to-noise ratios for far-field sta-
392 tions, it is difficult to determine at what point eq. (14) is no longer able to predict the observed
393 displacements; however, we settle on $t_{bd} = 0.8$ years after the earthquake, while acknowl-
394 edging that the choice is subjective. As noted in *Hines and Hetland* [2016], overestimating t_{bd}
395 will result in a bias towards overestimating η_{eff} , while picking a t_{bd} which is too low will not
396 necessarily result in a biased estimate of η_{eff} , although the uncertainties would be larger. We
397 can then consider inferences of η_{eff} to be an upper bound on the viscosity needed to describe
398 the far-field rate of deformation during the first 0.8 years of postseismic deformation.

401 We estimate coseismic slip, afterslip, and effective viscosities by solving

$$\min_{s, \eta_{eff}} \left(\left\| \frac{u_{pred}(s, \eta_{eff}) - u_{post}}{\sigma_{post}} \right\|_2^2 + \lambda_s \|s\|_2^2 + \lambda_\eta \|\nabla \eta_{eff}^{-1}\|_2^2 \right), \quad (15)$$

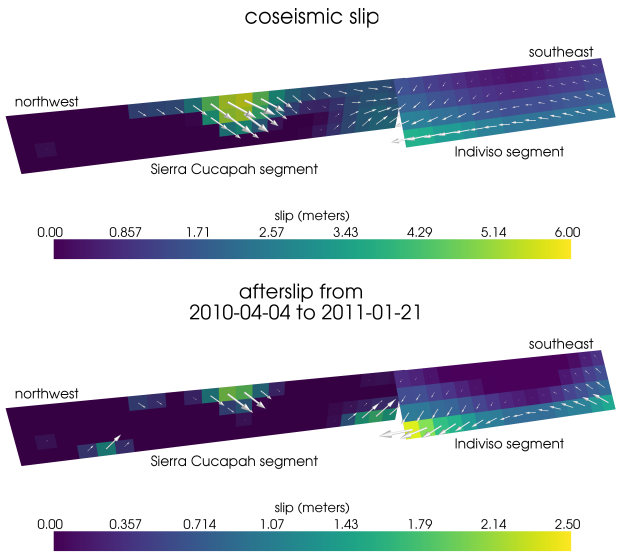
402 where u_{post} consists of the first 0.8 years of postseismic deformation and u_{pred} are the pre-
 403 dicted displacements from eq. (14). Due to inherent non-uniqueness, we have added zeroth-
 404 order Tikhonov regularization to estimates of s and second-order Tikhonov regularization to
 405 estimates of effective fluidity η_{eff}^{-1} . The degree to which we impose the regularization on slip
 406 and fluidity is controlled by the penalty parameters λ_s and λ_η , which are chosen with trade-
 407 off curves (Figure S1). Our goal is to get a prior constraint on η_{eff} to minimize the amount
 408 of searching we have to do when describing the postseismic deformation over the full five years,
 409 which we do in Section 3.3. Estimates of s made here will not be used in Section 3.3, and
 410 so the motivation behind adding regularization to s is to ensure that the slip driving viscoelas-
 411 tic relaxation in eq. (14) is sensible.

412 Our initial estimate for coseismic slip and cumulative afterslip over the first 0.8 years
 413 after the El Mayor-Cucapah earthquake are shown in Figure 11. Similar to our elastic slip model
 414 from Section 3.1, a significant amount of right-lateral and normal coseismic slip is inferred
 415 to be on the Sierra Cucapah segment. Our coseismic slip solution on the Sierra Cucapah seg-
 416 ment is consistent with field studies [Fletcher *et al.*, 2014] and the model from Wei *et al.* [2011b].
 417 Our inferred slip on the Indiviso fault segment differs from Wei *et al.* [2011b] because the GPS
 418 data used in this study is not capable of resolving the spatial distribution of fault slip on that
 419 segment (Figure S2). The potency of inferred coseismic slip is $3.3 \times 10^9 \text{ m}^3$, which is also
 420 about the same as that inferred from Section 3.1. The present inference of afterslip on the In-
 421 diviso fault is significantly less than what was found in the Section 3.1 where we did not ac-
 422 count for viscoelasticity. When fault slip is simultaneously estimated with viscosity, the po-
 423 tency of inferred afterslip over the first 0.8 years after the earthquake is $0.85 \times 10^9 \text{ m}^3$, com-
 424 pared to $3.5 \times 10^9 \text{ m}^3$ when we assume the crust and upper mantle are elastic. The signifi-
 425 cant amount of afterslip inferred on the Indiviso fault in Section 3.1 seems to be compensat-
 426 ing for unmodeled viscoelastic relaxation. The fact that there is still an appreciable amount
 427 of afterslip inferred on the Indiviso fault raises the question of whether it is compensating for
 428 viscoelastic relaxation that is more localized than what we allow for since we only estimate
 429 depth dependent variations in viscosity.

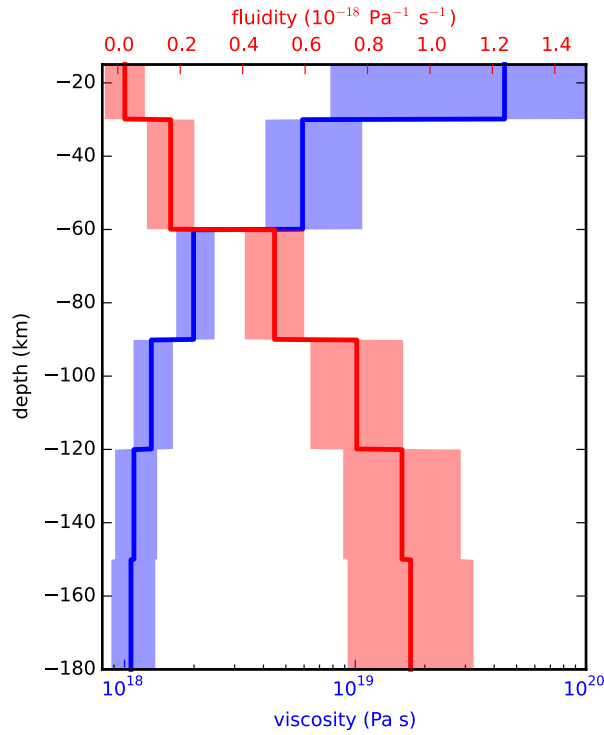
430 Our estimated effective viscosities, and corresponding fluidities, are shown in Figure 12.
 431 Although fluidity is rarely used in geophysical literature, eq. (13) is linear with respect to flu-
 432 idity and so the fluidity indicates the amplitude of the viscoelastic signal coming from each
 433 layer. We use bootstrapping to find the 95% confidence intervals for our estimated effective
 434 viscosities which are shown as shaded regions in Figure 12. It is important to remember that
 435 the presented effective viscosities were estimated with a smoothing regularization constraint
 436 and so the uncertainties are almost certainly underestimated [Aster *et al.*, 2011]. Indeed, many
 437 viscosity profiles which are outside of the shown confidence intervals can just as adequately
 438 described the first 0.8 years of postseismic deformation. Our solution in Figure 12 should be
 439 interpreted as the smoothest effective viscosity profile which is capable of describing the data.
 440 This means that any sharp viscosity transitions will be tapered out in the inversion, which we
 441 demonstrate with a synthetic test in Figure S2. Nonetheless, a robust feature that we see is that
 442 the largest jump in fluidity is at 60 km depth, which is consistent with the range of lithosphere-
 443 asthenosphere boundary depths inferred by Lekic *et al.* [2011]. This transitional depth is also
 444 consistent with the the viscosity structure required to explain far-field postseismic deforma-
 445 tion following the Hector Mine earthquake [Freed *et al.*, 2007]. We find that the viscosity be-
 446 low 60 km depth needs to be $\sim 1 \times 10^{18} \text{ Pa s}$ to describe the early rate of postseismic defor-
 447 mation at far-field stations while the lower crust and uppermost mantle need to be relatively
 448 stronger. The viscosity of the lower crust has the largest uncertainties because there is no ev-
 449 idence of relaxation in that layer, meaning that it is effectively elastic over the first 0.8 years
 450 after the earthquake.

456 3.3 Full Postseismic Inversion

457 In the previous section, we used the inverse method from Hines and Hetland [2016] to
 458 constrain the effective viscosity structure required to explain the first 0.8 years of postseismic



451 **Figure 11.** Coseismic slip and afterslip inferred by fitting eq. (14) to the first 0.8 years of postseismic
452 displacements.



453 **Figure 12.** Effective viscosities and associated fluidities inferred by fitting eq. (14) to the first 0.8 years of
454 postseismic displacements. 95% confidence intervals, estimated from bootstrapping, are indicated by shaded
455 regions.

459 deformation. In this section, we use these effective viscosities as a prior constraint when searching
 460 for models which are capable of describing the available five years of postseismic data,
 461 where our forward problem is now eq. (11) rather than the approximation given by eq. (14).
 462 We perform a series of fault slip inversions assuming a variety of rheologies for the lower crust
 463 and upper mantle which are consistent with our findings from Section 3.2. We appraise each
 464 model using the mean chi-squared value,

$$\bar{\chi}^2 = \frac{1}{N} \left\| \frac{u_{\text{pred}} - u_{\text{post}}}{\sigma_{\text{post}}} \right\|_2^2, \quad (16)$$

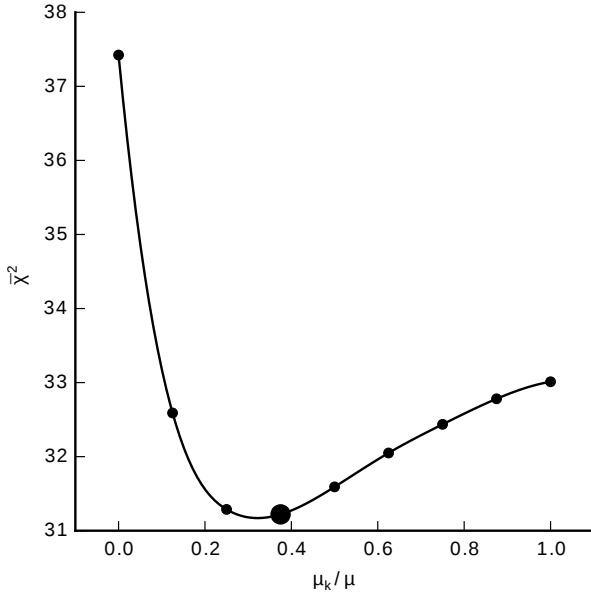
465 where N is the number of observations.

466 We first assume that the crust and mantle can be described with a Maxwell rheology,
 467 and we set the steady-state viscosity, η_M , equal to our inference of η_{eff} . We compute f and
 468 g from eq. (11) using Pylith, and we use the same spatial and temporal discretization of s as
 469 in Sections 3.1 and 3.2. We estimate s using linear least squares and find a misfit of $\bar{\chi}^2 =$
 470 37.4. For comparison, $\bar{\chi}^2 = 35.3$ for the elastic model from Section 3.1. The Maxwell vis-
 471 coelastic model has a larger misfit because it tends to overestimate the rate of deformation af-
 472 ter about three years (Figure 7). Since our initial estimates of η_{eff} may be biased towards over-
 473 estimating viscosities, we have also performed the slip inversion where we use uniformly lower
 474 viscosities in the crust and mantle; however, decreasing the viscosity only increases the mis-
 475 fit. Although, the viscosities used here are consistent with the successful Maxwell viscoelas-
 476 tic models found by *Rollins et al.* [2015] and *Spinler et al.* [2015], which had mantle viscosi-
 477 ties on the order of 10^{18} Pa s and relatively higher lower crustal viscosities, we find that such
 478 a model is incapable of describing the entire postseismic time series. *Pollitz et al.* [2001] sim-
 479 ilarly recognized this deficiency in a Maxwell rheology, which then motivated their exploration
 480 of a Burgers rheology upper mantle [*Pollitz*, 2003].

481 Instead of exploring a Burgers rheology mantle, which introduces two new parameters
 482 that need to be estimated, the transient viscosity, η_K , and transient shear modulus, μ_K , we first
 483 consider a Zener rheology for the mantle, which only introduces one unknown model param-
 484 eter, μ_K . We assume that the lower crust still has a Maxwell rheology. The steady-state vis-
 485 cosity in the crust and the transient viscosity in the mantle are set equal to the inferred effec-
 486 tive viscosities. We then estimate the ratio of shear moduli, $\frac{\mu_K}{\mu}$. We compute nine different
 487 sets of Green's functions, f and g , where we assume values of $\frac{\mu_K}{\mu}$ ranging from 0 to 1. The
 488 former being a degenerate case where the Zener model reduces to the above Maxwell model.
 489 We estimate coseismic slip and afterslip for each realization of $\frac{\mu_K}{\mu}$. We find that a shear mod-
 490 uli ratio of 0.375 yields the best prediction to the observed postseismic displacements with a
 491 misfit of $\bar{\chi}^2 = 31.2$ (Figure 13). The improvement in the Zener model over the Maxwell model
 492 can be seen in the fit to the far-field data (Figure 7) where the Zener model does a significantly
 493 better job at explaining the transient rate of deformation throughout the five years considered
 494 in this study. The rheologic parameters for our preferred Zener model are summarized in Ta-
 495 ble 1.

496 Because we are able to adequately describe the available five years of postseismic de-
 497 formation with a Zener model, we do not find it necessary to explore the parameter space for
 498 a more complicated Burgers rheology. However, since the Zener model is a Burgers model with
 499 an infinite steady-state viscosity, we can conclude that any Burgers rheology that has a tran-
 500 sient viscosity consistent with that found in Section 3.2 and a steady-state viscosity $\gtrsim 10^{20}$
 501 Pa s, which is effectively infinite on the time scale of five years, would also be able to sat-
 502 isfactorily describe the observable postseismic deformation.

503 The regularized inference of coseismic slip and afterslip for our preferred Zener model
 504 is shown in Figure 14. The inferred coseismic potency is 3.0×10^9 m³, equivalent to a Mw=7.26
 505 earthquake, where most of the slip is shallow and on the Sierra Cucapah fault segment. The
 506 potency of five years of afterslip is 1.1×10^9 m³. Most of the afterslip in our preferred model
 507 occurs within the first year after the earthquake and coincides with the location of our inferred



496 **Figure 13.** Mean chi-squared value for the best fitting slip model as a function of the transient shear modu-
 497 lus relative to the elastic shear modulus in a Zener upper mantle. Large dot indicates our preferred ratio.

510 coseismic slip. Inferred afterslip within the first year is accounting for the most rapid near-
 511 field transient deformation. After one year, afterslip is inferred to be deeper down on the Sierra
 512 Cucapah segment, which is describing much of the sustained near-field postseismic deforma-
 513 tion. We emphasize, that the GPS station closest to where we infer afterslip, P496, is still about
 514 30 km away, which is too far for us to conclusively argue for sustained localized deformation
 515 rather than shallow distributed deformation. The deep afterslip inferred after one year could
 516 potentially be describing deformation resulting from lower crustal flow. To test this, we have
 517 modified our preferred model by decreasing the lower crustal viscosity from 5.91×10^{19} Pa
 518 s to 1×10^{19} Pa s, which is still consistent with our viscosity inference from Section 3.2, and
 519 we inverted for fault slip. We find that a model with a weaker lower crust adequately describes
 520 the postseismic displacements without any afterslip after one year, while still requiring about
 521 the same amount of afterslip over the first year. We do believe that the early, shallow after-
 522 slip on the Sierra Cucapah segment is a robust feature in our preferred model, while we are
 523 not confident in our inference of later deep afterslip.

524 The postseismic displacements predicted by our preferred Zener model are shown in Fig-
 525 ures 4, 5 and 7. The largest misfit occur within the Imperial Valley and there does not appear
 526 to be any systematic trend in the residuals. This suggests that the large errors are due to lo-
 527 calized processes such as fault slip in the Imperial Valley triggered by the El Mayor-Cucapah
 528 earthquake [Wei *et al.*, 2011a, 2015]. We do not see any pattern in the residuals that would sug-
 529 gest a laterally heterogeneous viscosity structure, which has been explored by Pollitz *et al.* [2012]
 530 and Rollins *et al.* [2015]. We do notice regionally uniform seasonal oscillations in the lateral
 531 and vertical components of the residuals with an amplitude of 1-2 millimeters. This is the re-
 532 result of our method for data processing which is not able to completely remove the seasonal
 533 signal in the GPS data, which was discussed in Section 2. Additionally, we see systematic mis-
 534 fit in the later postseismic period west of the Landers and Hector Mine earthquakes, which may
 535 be the result of unmodeled postseismic deformation following those earthquakes. Lastly, there
 536 are clear discrepancies between the observed and predicted vertical displacements following
 537 the first year after the El Mayor-Cucapah earthquake. We observe a broad uplift throughout
 538 Southern California which is inconsistent with any postseismic model.

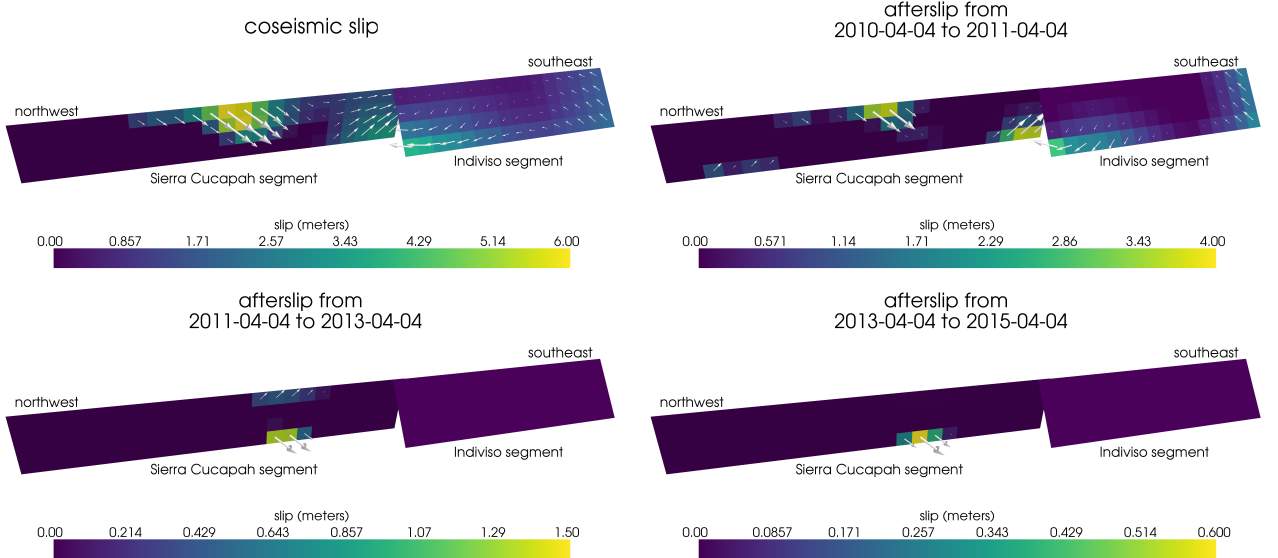


Figure 14. Inferred coseismic slip and afterslip when assuming a Maxwell rheology in the lower crust and a Zener rheology in the upper mantle. The transient viscosity η_K in the mantle and steady-state viscosity η_M in the crust are set equal to the effective viscosities from Figure 12. We set $\frac{\mu_K}{\mu} = 0.375$ in the upper mantle.

4 Discussion

It has long been recognized that deep afterslip and viscoelastic relaxation following an upper crustal earthquake can result in similar horizontal ground deformation at the surface [e.g. Savage, 1990; Pollitz *et al.*, 2001; Hearn, 2003; Feigl and Thatcher, 2006]. The similarity of the horizontal postseismic deformation results in a non-uniqueness in inferences of afterslip or viscoelastic relaxation. The spatial pattern of vertical postseismic deformation has been proposed to be a discriminant between deep afterslip and viscoelastic relaxation [e.g. Pollitz *et al.*, 2001; Hearn, 2003]. It is, however, important to note that patterns of vertical deformation are very sensitive to the depth-dependence of viscosity below the upper crust [Yang and Toksöz, 1981; Hetland and Zhang, 2014]. The similarity between deformation resulting from deep afterslip and viscoelastic relaxation of coseismic stresses is different from the ill-posedness described in Section 3.2. In our method, any inferred afterslip will also mechanically drive additional viscoelastic relaxation. The horizontal deformation resulting from deep afterslip will generally be in the opposite direction as horizontal deformation resulting from viscoelastic relaxation of subsequent stresses in the lower crust (Figure 9). As a result, there is a trade-off between inferences of deep afterslip and lower crustal viscosity. In our synthetic tests in Hines and Hetland [2016], we have found that inverting surface deformation for afterslip and viscosity within the same depth interval tends to result in overestimated afterslip and an underestimated viscosity.

Most postseismic studies assume Maxwell viscoelasticity in the lower crust and upper mantle [e.g. Nur and Mavko, 1974; Pollitz *et al.*, 2000; Hetland, 2003; Freed *et al.*, 2006; Johnson *et al.*, 2009; Hearn *et al.*, 2009], which is the simplest viscoelastic rheologic model. In Southern California, postseismic studies following the Landers [Pollitz *et al.*, 2000], Hector Mine [Pollitz *et al.*, 2001], and El Mayor-Cucapah earthquake [Spinler *et al.*, 2015; Rollins *et al.*, 2015], have assumed Maxwell viscoelasticity in the lower crust and upper mantle and have inferred upper mantle viscosities on the order of 10^{17} to 10^{18} Pa s and lower crust viscosities $\gtrsim 10^{19}$ Pa s. These postseismic studies are consistent with Kaufmann and Amelung [2000] and Cavalié *et al.* [2007], who found that an upper mantle viscosity of 10^{18} Pa s and a crustal viscos-

570 ity $\gtrsim 10^{20}$ Pa s are necessary to describe subsidence resulting from changes in loading from
 571 Lake Mead. This isostatic adjustment is a process with similar spatial and temporal scales as
 572 postseismic deformation, and thus the inferred viscosities of these two types of studies would
 573 likely agree. While these studies found viscosities that are consistent with our effective vis-
 574 cosities from Section 3.2, they are inconsistent with viscosity estimates made from geophys-
 575 ical processes that occur over longer time scales. For example, *Lundgren et al.* [2009] found
 576 that lower crust and upper mantle viscosities on the order of 10^{21} and 10^{19} Pa s, respectively,
 577 are needed to describe interseismic deformation along the Southern San Andreas fault zone
 578 in the Salton Sea region. An even higher mantle viscosity, on the order of 10^{20} Pa s, is re-
 579 quired to describe isostatic adjustment resulting from the draining of Lake Bonneville, which
 580 occurs on the time scales of 10^4 years [*Crittenden*, 1967; *Bills and May*, 1987].

581 An additional deficiency with the Maxwell rheology is that it predicts a steady decay
 582 in the rate of postseismic deformation over time, which fails to describe the commonly ob-
 583 served rapid, early transience followed by a relatively steady rate of postseismic deformation.
 584 One could explain the early transient postseismic deformation with fault creep and the later
 585 phase with relaxation in a Maxwell viscoelastic lower crust and upper mantle [e.g. *Hearn et al.*,
 586 2009; *Johnson et al.*, 2009]. However, postseismic deformation at distances greater than ~ 200
 587 km from the El Mayor-Cucapah epicenter can only be attributed to viscoelastic relaxation [e.g.
 588 *Freed et al.*, 2007] and we have demonstrated that the far-field deformation cannot be explained
 589 with a Maxwell rheology (Figure 7).

590 We found that a Zener rheology in the upper mantle with a transient viscosity of $\sim 10^{18}$
 591 Pa s does a noticeably better job at predicting far-field postseismic deformation. A general-
 592 ization of the Zener viscoelastic model, schematically represented as several Kelvin elements
 593 connected in series, is commonly used to describe seismic attenuation [*Liu et al.*, 1976]. The
 594 highest viscosity needed to describe seismic attenuation is on the order of 10^{16} Pa s [*Yuen and*
 595 *Peltier*, 1982] which has a characteristic relaxation time on the order of days. Even though
 596 our inferred transient viscosity is orders of magnitude larger than that required for seismic at-
 597 tenuation models, the two models are not incompatible. Rather, the delayed elasticity in seis-
 598 mic attenuation models occurs on such short time scales that it can be considered part of the
 599 instantaneous elastic phase of deformation associated with the preferred Zener model in this
 600 study.

601 Of course, a Zener rheology provides an incomplete description of the asthenosphere be-
 602 cause it does not have the fluid-like behavior required to explain isostatic rebound or convec-
 603 tion in the mantle [*O'Connell*, 1971]. *Yuen and Peltier* [1982] proposed a Burgers rheology
 604 with a low transient viscosity ($\eta_K \approx 10^{16}$ Pa s) and high steady-state viscosity ($\eta_M \approx 10^{21}$
 605 Pa s) to describe both seismic attenuation and long term geologic processes. The justification
 606 of a Burger's rheology mantle is further supported by laboratory experiments on olivine [*Chopra*,
 607 1997]. *Pollitz* [2003] sought to describe postseismic deformation following Hector Mine with
 608 a Burgers rheology mantle and they found a best fitting transient viscosity of 1.6×10^{17} Pa
 609 s and steady-state viscosity of 4.6×10^{18} Pa s. While the Burgers rheology was introduced
 610 as a means of bridging the gap between relaxation observed in long and short term geophys-
 611 ical processes, the inferred steady state viscosity from *Pollitz* [2003] is still inconsistent with
 612 the Maxwell viscosities inferred from studies on the earthquake cycle and Lake Bonneville.
 613 The transient viscosity inferred by *Pollitz* [2003] is constrained by the earliest phase of post-
 614 seismic deformation following the Hector Mine earthquake. While *Pollitz* [2003] ruled out deep
 615 afterslip as an alternative mechanism based on inconsistent vertical deformation, it is still pos-
 616 sible to successfully describe all components of early postseismic deformation following the
 617 Hector Mine earthquake with afterslip at seismogenic depths [*Jacobs et al.*, 2002]. It is then
 618 possible that the preferred rheologic model from *Pollitz* [2003] was biased towards inferring
 619 a particularly low transient viscosity by neglecting to account for afterslip. This is in contrast
 620 to the present study, where we have inferred a viscosity structure simultaneously with after-
 621 slip. We also argue that a transient rheology is necessary to explain postseismic deformation;
 622 however, our preferred transient viscosity of $\sim 10^{18}$ Pa s in the upper mantle is an order of mag-

623 nitude larger than the transient viscosity found by Pollitz [2003]. The transient viscosity in-
 624 ferred here is consistent with the results of Pollitz [2015], who reanalyzed postseismic data
 625 following the Landers and Hector Mine earthquake allowing the first few months of transient
 626 deformation to be described by afterslip. Since a Zener model is able to describe the avail-
 627 able postseismic deformation following the El Mayor-Cucapah earthquake, any Burgers rhe-
 628 ology with a steady-state viscosity that is $\gtrsim 10^{20}$ Pa s, effectively infinite over five years, would
 629 also be able to describe the postseismic deformation. Such a Burgers model might then be con-
 630 sistent with the steady-state viscosities necessary for lake loading, interseismic deformation,
 631 and mantle dynamics.

632 5 Conclusion

633 We have extracted a smoothed estimate of postseismic deformation following the El Mayor-
 634 Cucapah earthquake from GPS displacement time series. Our estimated postseismic deforma-
 635 tion reveals far-field (epicentral distances $\gtrsim 200$ km) transient deformation which is undetectable
 636 after about three years. Near-field deformation exhibits transience that decays to a sustained,
 637 elevated rate after about one or two years. We found that near-field transient deformation can
 638 be explained with shallow afterslip, and the sustained rate of near-field deformation can ei-
 639 ther be explained with continued afterslip or viscoelastic relaxation in the lower crust. Far-field
 640 transient deformation can be more definitively ascribed to viscoelastic relaxation at depths greater
 641 than ~ 60 km. Beneath that depth, a transient viscosity of $\sim 1 \times 10^{18}$ Pa s is required to de-
 642 scribe the rate of far-field deformation throughout the five years considered in this study. By
 643 describing the available postseismic deformation with a transient rheology in the mantle, our
 644 preferred model does not conflict with the generally higher steady-state viscosities inferred from
 645 geophysical processes occurring over longer time scales.

646 Acknowledgements

647 We thank Andy Freed for an illuminating discussion on the data used in this study. We
 648 also thank F. Pollitz and an anonymous reviewer for comments that improved this manuscript,
 649 and Editor Martha Savage. This material is based on EarthScope Plate Boundary Observatory
 650 data services provided by UNAVCO through the GAGE Facility with support from the Na-
 651 tional Science Foundation (NSF) and National Aeronautics and Space Administration (NASA)
 652 under NSF Cooperative Agreement No. EAR-1261833. The data used in this study can be found
 653 at www.unavco.org. This material is based upon work supported by the National Science Foun-
 654 dation under Grant Numbers EAR 1045372 and EAR 1245263.

655 References

- 656 Aagaard, B. T., M. G. Knepley, and C. A. Williams (2013). A domain decomposition
 657 approach to implementing fault slip in finite-element models of quasi-static and dy-
 658 namic crustal deformation, *Journal of Geophysical Research: Solid Earth*, 118, doi:
 659 10.1002/jgrb.50217.
- 660 Argus, D. F., M. B. Heflin, G. Peltzer, F. Crampé, and F. H. Webb (2005), Interseismic
 661 strain accumulation and anthropogenic motion in metropolitan Los Angeles, *Journal of*
 662 *Geophysical Research: Solid Earth*, 110(4), 1–26, doi:10.1029/2003JB002934.
- 663 Aster, R. C., B. Borchers, and C. H. Thurber (2011), Parameter Estimation and Inverse
 664 Problems, vol. 90, Academic Press.
- 665 Bawden, G. W., W. Thatcher, R. S. Stein, K. W. Hudnut, and G. Peltzer (2001), Tectonic
 666 contraction across Los Angeles after removal of groundwater pumping effects., *Nature*,
 667 412(August), 812–815, doi:10.1038/35090558.
- 668 Bills, B. G., and G. M. May (1987), Lake Bonneville: Constraints on Lithospheric Thick-
 669 ness and Upper Mantle Viscosity From Isostatic Warping of Bonneville, Provo, and
 670 Gilbert Stage Shorelines, *Journal of Geophysical Research-Solid Earth and Planets*,

- 671 92(B11), 11,493–11,508, doi:10.1029/JB092iB11p11493.
- 672 Çakir, Z., S. Ergintav, H. Özener, U. Dogan, A. M. Akoglu, M. Meghraoui, and
673 R. Reilinger (2012), Onset of aseismic creep on major strike-slip faults, *Geology*,
674 40(12), 1115–1118, doi:10.1130/G33522.1.
- 675 Cavalié, O., M. P. Doin, C. Lasserre, and P. Briole (2007), Ground motion measurement in
676 the Lake Mead area, Nevada, by differential synthetic aperture radar interferometry time
677 series analysis: Probing the lithosphere rheological structure, *Journal of Geophysical*
678 *Research: Solid Earth*, 112(3), 1–18, doi:10.1029/2006JB004344.
- 679 Cetin, E., Z. Çakir, M. Meghraoui, S. Ergintav, and A. M. Akoglu (2014), Extent and
680 distribution of aseismic slip on the İsmetpaşa segment of the North Anatolian Fault
681 (Turkey) from Persistent Scatterer InSAR, *Geochemistry, Geophysics, Geosystems*, 15,
682 doi:10.1002/2014GC005307. Received.
- 683 Chopra, P. N. (1997), High-temperature transient creep in olivine rocks, *Tectonophysics*,
684 279, 93–111, doi:10.1016/S0040-1951(97)00134-0.
- 685 Crittenden, M. (1967), Viscosity and Finite Strength of the Mantle as Determined from
686 Water and Ice Loads*, *Geophysical Journal of the Royal Astronomical* ..., pp. 261–279,
687 doi:10.1111/j.1365-246X.1967.tb06243.x.
- 688 Davis, J. L., B. P. Wernicke, and M. E. Tamisiea (2012), On seasonal signals in geode-
689 tic time series, *Journal of Geophysical Research: Solid Earth*, 117(1), 1–10, doi:
690 10.1029/2011JB008690.
- 691 Feigl, K. L., and W. Thatcher (2006), Geodetic observations of post-seismic transients in
692 the context of the earthquake deformation cycle, *Comptes Rendus - Geoscience*, 338,
693 1012–1028, doi:10.1016/j.crte.2006.06.006.
- 694 Fletcher, J. M., O. J. Teran, T. K. Rockwell, M. E. Oskin, K. W. Hudnut, K. J. Mueller,
695 R. M. Spelz, S. O. Akciz, E. Masana, G. Faneros, E. J. Fielding, S. Leprince, A. E.
696 Morelan, J. Stock, D. K. Lynch, A. J. Elliott, P. Gold, J. Liu-Zeng, A. González-
697 Ortega, A. Hinojosa-Corona, and J. González-García (2014), Assembly of a large
698 earthquake from a complex fault system: Surface rupture kinematics of the 4 April
699 2010 El Mayor-Cucapah (Mexico) Mw 7.2 earthquake, *Geosphere*, 10(4), 797–827,
700 doi:10.1130/GES00933.1.
- 701 Freed, A. M., R. Bürgmann, E. Calais, J. Freymueller, and S. Hreinsdóttir (2006), Impli-
702 cations of deformation following the 2002 Denali, Alaska, earthquake for postseismic
703 relaxation processes and lithospheric rheology, *Journal of Geophysical Research: Solid*
704 *Earth*, 111, 1–23, doi:10.1029/2005JB003894.
- 705 Freed, A. M., R. Bürgmann, and T. Herring (2007), Far-reaching transient motions after
706 Mojave earthquakes require broad mantle flow beneath a strong crust, *Geophysical*
707 *Research Letters*, 34, 1–5, doi:10.1029/2007GL030959.
- 708 Gonzalez-Ortega, A., Y. Fialko, D. Sandwell, F. A. Nava-pichardo, J. Fletcher,
709 J. Gonzalez-garcia, B. Lipovsky, M. Floyd, and G. Funning (2014), El Mayor-
710 Cucapah (Mw7.2) earthquake: early near-field postseismic deformation from In-
711 Sar and GPS observations, *Journal of Geophysical Research*, 119, 1482–1497, doi:
712 10.1002/2013JB010193. Received.
- 713 Hauksson, E., J. Stock, K. Hutton, W. Yang, J. A. Vidal-Villegas, and H. Kanamori
714 (2011), The 2010 Mw 7.2 El mayor-cucapah earthquake sequence, Baja Califor-
715 nia, Mexico and Southernmost California, USA: Active seismotectonics along the
716 Mexican pacific margin, *Pure and Applied Geophysics*, 168(3918), 1255–1277, doi:
717 10.1007/s00024-010-0209-7.
- 718 Hearn, E. H. (2003), What can GPS data tell us about the dynamics of post-seismic defor-
719 mation ?, (2003), 753–777.
- 720 Hearn, E. H., S. McClusky, S. Ergintav, and R. E. Reilinger (2009), Izmit earthquake post-
721 seismic deformation and dynamics of the North Anatolian Fault Zone, *Journal of Geo-*
722 *physical Research: Solid Earth*, 114(August 2008), 1–21, doi:10.1029/2008JB006026.
- 723 Hetland, E. A. (2003), Postseismic relaxation across the Central Nevada Seismic Belt,
724 *Journal of Geophysical Research*, 108(Figure 2), 1–13, doi:10.1029/2002JB002257.

- Hetland, E. A., and G. Zhang (2014), Effect of shear zones on post-seismic deformation with application to the 1997 Mw 7.6 manyi earthquake, *Geophysical Journal International*, **198**, 259–269, doi:10.1093/gji/ggu127.
- Hines, T. T., and E. A. Hetland (2013), Bias in estimates of lithosphere viscosity from interseismic deformation, *Geophysical Research Letters*, **40**(16), 4260–4265, doi:10.1002/grl.50839.
- Hines, T. T., and E. A. Hetland (2016), Rapid and simultaneous estimation of fault slip and heterogeneous lithospheric viscosity from post-seismic deformation, *Geophysical Journal International*, **204**(1), 569–582, doi:10.1093/gji/ggv477.
- Jacobs, A., D. Sandwell, Y. Fialko, and L. Sichoux (2002), The 1999 (Mw7.1) Hector Mine, California, Earthquake: Near-Field Postseismic Deformation from ERS Interferometry, *Bulletin of the Seismological Society of America*, **92**(May), 1433–1442.
- Johnson, K. M., and P. Segall (2004), Viscoelastic earthquake cycle models with deep stress-driven creep along the San Andreas fault system, *Journal of Geophysical Research: Solid Earth*, **109**, 1–19, doi:10.1029/2004JB003096.
- Johnson, K. M., R. Bürgmann, and J. T. Freymueller (2009), Coupled afterslip and viscoelastic flow following the 2002 Denali Fault, Alaska earthquake, *Geophysical Journal International*, **176**(3), 670–682, doi:10.1111/j.1365-246X.2008.04029.x.
- Jónsson, S., P. Segall, R. Pedersen, and G. Bjornsson (2003), Post-earthquake ground movements correlated to pore-pressure transients, *Nature*, **424**(July), 179–183, doi:10.1038/nature01758.1.
- Kaufmann, G., and F. Amelung (2000), Reservoir-induced deformation and continental rheology in vicinity of Lake Mead, Nevada, *Journal of Geophysical Research*, **105**(B7), 16,341, doi:10.1029/2000JB900079.
- Kroll, K. A., E. S. Cochran, K. B. Richards-Dinger, and D. F. Sumy (2013), Aftershocks of the 2010 Mw 7.2 El Mayor-Cucapah earthquake reveal complex faulting in the Yuha Desert, California, *Journal of Geophysical Research: Solid Earth*, **118**(October), 6146–6164, doi:10.1002/2013JB010529.
- Lekic, V., S. W. French, and K. M. Fischer (2011), Lithospheric Thinning Beneath Rifted Regions of Southern California, *Science*, **334**(November), 783–787.
- Liu, H.-P., D. L. Anderson, and H. Kanamori (1976), Velocity dispersion due to anelasticity; implications for seismology and mantle composition, *Geophysical Journal International*, **47**(1), 41–58, doi:10.1111/j.1365-246X.1976.tb01261.x.
- Lundgren, P., E. A. Hetland, Z. Liu, and E. J. Fielding (2009), Southern San Andreas-San Jacinto fault system slip rates estimated from earthquake cycle models constrained by GPS and interferometric synthetic aperture radar observations, *Journal of Geophysical Research: Solid Earth*, **114**(2), 1–18, doi:10.1029/2008JB005996.
- McGuire, J. J., and P. Segall (2003), Imaging of aseismic fault slip transients recorded by dense geodetic networks, *Geophysical Journal International*, **155**(3), 778–788, doi:10.1111/j.1365-246X.2003.02022.x.
- Meade, B. J., and B. H. Hager (2005), Block models of crustal motion in southern California constrained by GPS measurements, *Journal of Geophysical Research B: Solid Earth*, **110**, 1–19, doi:10.1029/2004JB003209.
- Murray, J. R., and P. Segall (2005), Spatiotemporal evolution of a transient slip event on the San Andreas fault near Parkfield, California, *Journal of Geophysical Research : Solid Earth*, **110**(9), 1–12, doi:10.1029/2005JB003651.
- Nur, A., and G. Mavko (1974), Postseismic viscoelastic rebound, *Science*, **183**(4121), 204–206, doi:10.1038/098448b0.
- O'Connell, R. J. (1971), Rheology of the Mantle, *EOS, Transactions, American Geophysical Union*, **52**, 140–142.
- Oskin, M. E., J. R. Arrowsmith, A. Hinojosa Corona, A. J. Elliott, J. M. Fletcher, E. J. Fielding, P. O. Gold, J. J. Gonzalez Garcia, K. W. Hudnut, J. Liu-Zeng, and O. J. Teran (2012), Near-field deformation from the El Mayor-Cucapah earthquake revealed by differential LIDAR, *Science*, **335**(6069), 702–705, doi:10.1126/science.1213778.

- Pollitz, F., C. Wicks, and W. Thatcher (2001), Mantle Flow Beneath a Continental Strike-Slip Fault : Postseismic Deformation After the 1999 Hector Mine Earthquake, *Science*, 1814(2001), 1814–1818, doi:10.1126/science.1061361.
- Pollitz, F. F. (2003), Transient rheology of the uppermost mantle beneath the Mojave Desert, California, *Earth and Planetary Science Letters*, 215, 89–104, doi: 10.1016/S0012-821X(03)00432-1.
- Pollitz, F. F., G. Peltzer, and R. Bürgmann (2000), Mobility of continental mantle: Evidence from postseismic geodetic observations following the 1992 Landers earthquake, *Journal of Geophysical Research*, 105(1999), 8035, doi:10.1029/1999JB900380.
- Pollitz, F. F., R. Bürgmann, and W. Thatcher (2012), Illumination of rheological mantle heterogeneity by the M7.2 2010 El Mayor-Cucapah earthquake, *Geochemistry, Geophysics, Geosystems*, 13(6), 1–17, doi:10.1029/2012GC004139.
- Pollitz, F. F. (2015). Postearthquake relaxation evidence for laterally variable viscoelastic structure and water content in the Southern California mantle, *Journal of Geophysical Research: Solid Earth*, 120, 2672–2696, doi:10.1002/2014JB011603.
- Rauch, H. E., F. Tung, and C. T. Striebel (1965), Maximum likelihood estimates of linear dynamic systems, *AIAA Journal*, 3(8), 1445–1450.
- Riva, R. E. M., and R. Govers (2009), Relating viscosities from postseismic relaxation to a realistic viscosity structure for the lithosphere, *Geophysical Journal International*, 176, 614–624, doi:10.1111/j.1365-246X.2008.04004.x.
- Rollins, C., S. Barbot, and J.-P. Avouac (2015), Postseismic Deformation Following the 2010 M7.2 El Mayor-Cucapah Earthquake : Observations , Kinematic Inversions , and Dynamic Models, *Pure and Applied Geophysics*, doi:10.1007/s00024-014-1005-6.
- Savage, J. C. (1990), Equivalent strike-slip earthquake cycles in half-space and lithosphere-asthenosphere earth models, *Journal of Geophysical Research*, 95, 4873, doi:10.1029/JB095iB04p04873.
- Savage, J. C., and J. L. Svart (2009), Postseismic relaxation following the 1992 M 7.3 Landers and 1999 M 7.1 Hector Mine earthquakes , southern California, *Journal of Geophysical Research*, 114(B01401), doi:10.1029/2008JB005938.
- Savage, J. C., J. L. Svart, and S. B. Yu (2005), Postseismic relaxation and transient creep, *Journal of Geophysical Research: Solid Earth*, 110, 1–14, doi:10.1029/2005JB003687.
- Segall, P., and M. Mathews (1997), Time dependent inversion of geodetic data, *Journal of Geophysical Research*, 102.
- Spinler, J. C., R. A. Bennett, C. Walls, L. Shawn, and J. J. G. Garcia (2015), Assessing long-term postseismic deformation following the M7.2 4 April 2010, El Mayor-Cucapah earthquake with implications for lithospheric rheology in the Salton Trough, *Journal of Geophysical Research: Solid Earth*, 120, 3664–3679, doi: 10.1002/2014JB011613.Received.
- Wei, M., D. Sandwell, Y. Fialko, and R. Bilham (2011a), Slip on faults in the Imperial Valley triggered by the 4 April 2010 Mw 7.2 El Mayor-Cucapah earthquake revealed by InSAR, *Geophysical Research Letters*, 38(January), 1–6, doi:10.1029/2010GL045235.
- Wei, M., Y. Liu, Y. Kaneko, J. J. McGuire, and R. Bilham (2015), Dynamic triggering of creep events in the Salton Trough, Southern California by regional M5.4 earthquakes constrained by geodetic observations and numerical simulations, *Earth and Planetary Science Letters*, 427, 1–10, doi:10.1016/j.epsl.2015.06.044.
- Wei, S., E. Fielding, S. Leprince, A. Sladen, J.-P. Avouac, D. Helmberger, E. Hauksson, R. Chu, M. Simons, K. Hudnut, T. Herring, and R. Briggs (2011b), Superficial simplicity of the 2010 El MayorCucapah earthquake of Baja California in Mexico, *Nature Geoscience*, 4(9), 615–618, doi:10.1038/ngeo1213.
- Yang M., and M. N. Toksöz (1981), Time-dependent deformation and stress relaxation after strike-slip earthquakes, *Journal of Geophysical Research*, 86, 2889–2901.
- Yuen, D. A., and W. R. Peltier (1982), Normal modes of the viscoelastic earth, *Geophysical Journal of the Royal Astronomical Society*, 69, 495–526, doi:10.1111/j.1365-246X.1982.tb04962.x.